Effects of Spatial Resolution,Land-Cover Heterogeneity and Different Classification Methods on Accuracy of Land-Cover Mapping

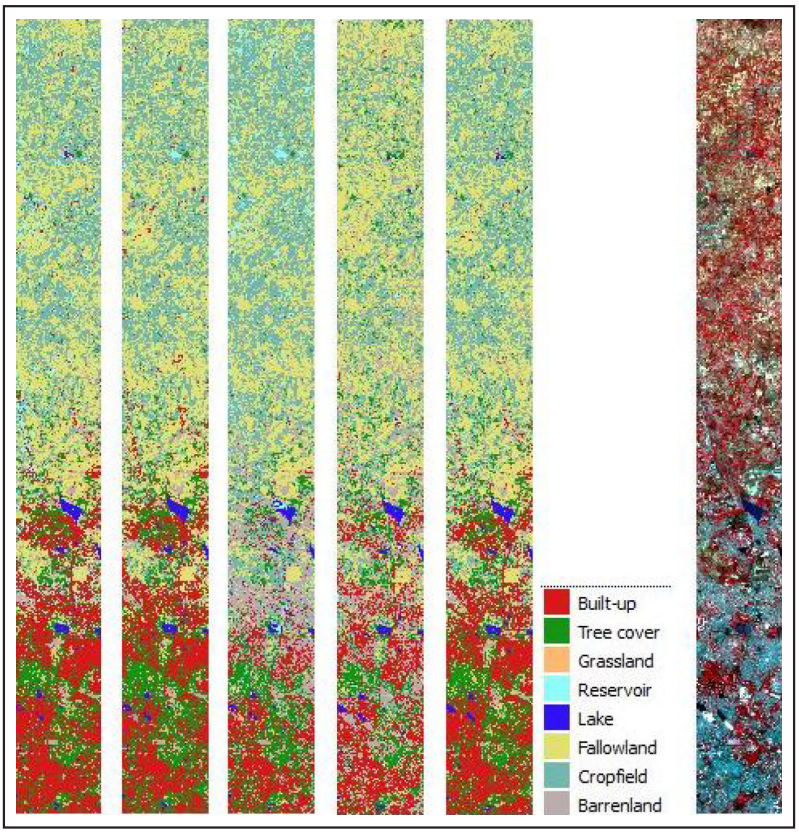

Kwame Tweneboa Awuah

Supervisors: Nils Nölke, Chair of Forest Inventory and Remote Sensing, Georg-August Universität, Göttingen
Eric Agestam, SLU Southern Swedish Forest Research Center

Swedish University of Agricultural Sciences

Master Thesis no. 287

Southern Swedish Forest Research Centre

Alnarp 2017

Effects of Spatial Resolution,Land-Cover Heterogeneity and Different Classification Methods on Accuracy of Land-Cover Mapping

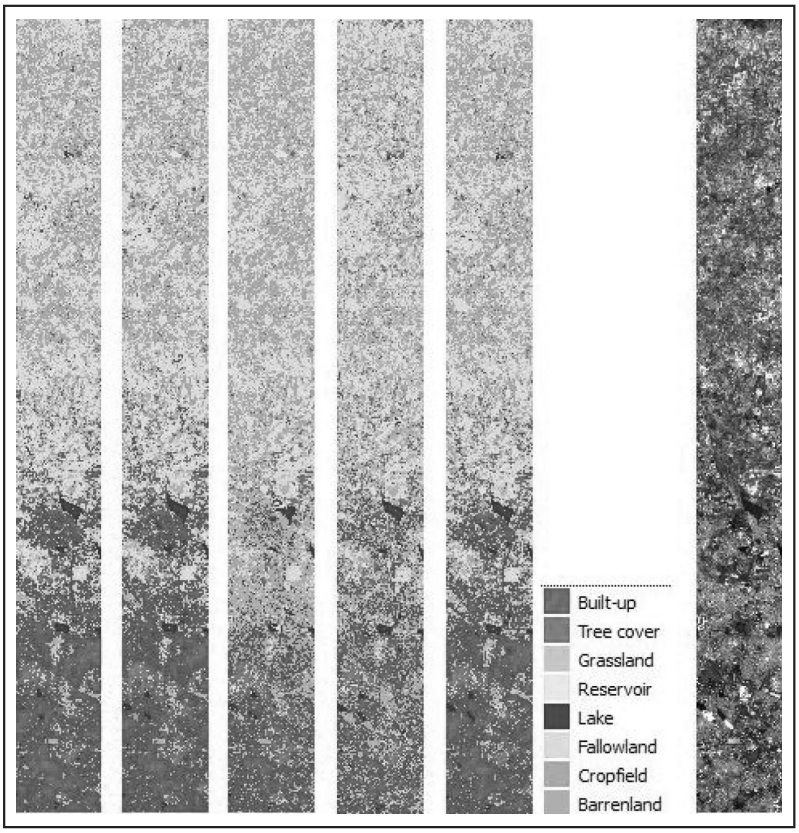

Kwame Tweneboa Awuah

Supervisors: Nils Nölke, Chair of Forest Inventory and Remote Sensing, Georg-August Universität, Göttingen
Eric Agestam, SLU Southern Swedish Forest Research Center

Examiner: Per Magnus Ekö, SLU Southern Swedish Forest Research Center

Swedish University of Agricultural Sciences
Master Thesis no. 287
Southern Swedish Forest Research Centre
Alnarp 2017

Master thesis in Forest Management,
Advanced Level (A2E), SLU course code EX0630, 30 ECTS

ABSTRACT

Despite improved spatial and spectral characteristics of satellite and aerial imaging systems, land-cover classification is still challenged by a continuously evolving and complex rural and urban landscape conditions resulting from diverse land-use scenarios. Sizes and material composition of impervious surfaces changes greatly from urban to rural areas, leading to varying spectral signatures and ultimately misclassification. This creates a challenge in choosing suitable classification algorithms and image processing methods. In this study, the influence of spatial resolution and land-cover spectral and spatial heterogeneity on accuracy of land-cover classification at a rural-urban interface was examined alongside comparison of Random Forest (RF) and Support Vector Machine (SVM) classification algorithms. Further, the performance of spectral unmixing strategies was tested against standard feature extraction methods, namely, NAPCA and PCA. The results showed a 10 % improvement in classification accuracy from 30 m to 10 m spatial resolution for both overall accuracy and Kappa coefficients, however, relatively high per-pixel class disagreement (39 %) was recorded between the different resolution maps, pointing to the fact that overall accuracy or Kappa coefficients may not capture the spatial resolution effects on classification accuracy results in its entirety. SVM classifier proved superior to the RF classifier with even a relatively bigger margin at the coarser spatial resolution (i.e. 4.9 % and 5.7 % higher accuracy at 10 m and 30 m spatial resolution respectively). Higher classification accuracies were observed for partial unmixing and sum-to-unity unmixing feature extraction strategies at both spatial resolutions relative to the results from PCA, NAPCA and original image data (i.e. 62 %, 61 %, 51 %, 61 % and 59 % respectively for 30 m resolution, and, 67 %, 67 %, 62 %, 65 % and 66 % respectively for 10 m resolution image). It was found that the dominance of unmixing-based feature extraction methods reduced while the standard dimensionality reduction approaches (NAPCA and PCA) made a zero contribution to improving classification accuracy at finer spatial resolution (i.e. 10 m). According to the results of land-cover heterogeneity assessment, more fragmented and spatially diverse landscapes were comparably more spectrally diverse along the rural-urban gradient. A high degree of landscape heterogeneity and lowest classification accuracy was observed in the peri-urban region at approximately 11 kilometers from the very urban area. The findings indicate that landscapes with high PD, LSI, SHDI and low CONTAG have lower accuracy while homogeneous and less fragmented landscapes have higher accuracy. The findings from the study will provide a basis for more accurate time series analysis of land-use dynamics at the rural-urban interface.

Keywords: *Image classification, spatial resolution, heterogeneity, support vector machine (SVM), random forest (RF), spectral unmixing, feature extraction, endmember extraction.*

Table of Content

1 Introduction

1.1 Background and Relevance

Analyses of land use changes and their effects on sustainable management of natural resources requires a good information base on the patterns and dynamics in land-cover at different spatial and temporal scales. For this reason satellite remote sensing data have become very instrumental especially with recent advances in optical satellite imaging systems (Chassot et al. 2011; Benediktsson et al. 2012; Jensen 2015; Dash and Ogutu 2016; Khorram et al. 2016). Such data often shows the spectral characteristics of land surface features. Suitably, these should be converted into thematic form to aid the extraction of relevant information. As such, classification of remotely sensed images is a popular and a very instructive method for organizing land cover and land use information in the form of thematic maps.

Accuracy of land-cover maps has for long being a pertinent issue for image classification processes, however, in the recent past, information on map accuracy have particularly received wider attention with the increasing consensus on understanding and monitoring of global environmental change, and coordination of mitigation and adaptation actions (Mora et al. 2014). For instance, accurate characterization of land-cover is vital for studying climate change, biodiversity and carbon cycle (Hackman et al. 2017). Additionally, land-cover datasets serve as inputs in many ecosystem models, regional and global climate simulation models, global circulation models, land surface models (Mora et al 2014; Fritz et al. 2011) and socio-economic models (Nesbitt and Meitner 2016; Schüle et al. 2017). Thus, consistent and accurate land cover data are in high demand since the quality of selected land-cover datasets has a remarkable influence on model results (Benitez et al 2004; Sertel et al 2010). Accordingly, techniques that overcome common sources of classification error and provide optimally accurate results will gain significance.

In fast developing megacities, rapid changes in land-use and land-cover are evident in both urban and rural areas. Further, same land-cover types, particularly green spaces tend to assume considerably different functions along rural-urban interface. For example, ecological and production functions are predominant at rural frontiers, whereas urban centers are associated with recreational functions. It has been hypothesized that these variations in the functioning and configuration of green spaces exhibit similar patterns over space and time and also reflects socioeconomic features in surrounding landscapes (Simon 2008). As part of a project (FOR2432/1) to test this hypothesis in the Indian megacity of Bangalore, the general idea of this study is therefore to explore and test options for land-cover classification that ensures more accurate time series analysis of land-use dynamics at the rural-urban interface.

1.2 Image Classification and Accuracy Assessment

Classification accuracy refers to how well a particular map label describes earth surface features (Al-doski et al. 2013). A typical example is whether a wheat field is correctly labeled as cropland or classified wrongly as grassland. Errors in classification are therefore discrepancies between ground reality and its representation on a thematic map (Foody 2002).

Accuracy assessment is conducted by identifying and evaluating map errors (Congalton and Green 2008). Congalton (2001) identifies four main ways to progressively investigate map accuracy, and are regarded as the major historical stages in accuracy assessment (Foody 2002). These include visual inspection, non-site specific analysis, difference image creation and quantitative accuracy assessment.

Initially, accuracy assessment was restricted to basic visual appraisal, and maps were regarded as accurate if they 'looked good' to the analyst. This step of accuracy assessment is subjective and considered insufficient or inappropriate as the concluding step (Foody, 2002). Meanwhile, it is very essential to visually assess maps in order to justify further accuracy assessment steps (Congalton, 2001). The second stage of accuracy assessment was aimed at a more objective way of quantifying classification accuracy. The analysis only involved a comparison of the extent of area occupied by classes in the derived map in relation to a reference dataset assumed to be error free (Foody, 2002). However a major limitation to this approach of accuracy assessment is its disregard for any location component (Congalton, 2001). The difference image creation approach involves accuracy metrics derivation from a direct comparison of two registered images (Congalton, 2001). When the comparison is between a derived map and reference map, the process returns the proportion of same class pixels that are in agreement in both maps. This is usually referred to as the overall map accuracy. Such comparison can also be between images or maps of the same area occurring at different points in time, and, maps from different analyst using same dated images. In the former case, the difference is regarded as changes over time whereas the latter shows differences in methodology used by the different analysts (Congalton, 2001).

The quantitative accuracy assessment stage is essentially a modification or improvement of the third. This involves a deeper assessment of information on the agreement of derived and reference map labels. The results are usually reported in the form of a contingency table or error matrix. The error matrix is an array of numbers displayed in rows and columns which represent the number of sample units (i.e. pixels, cluster of pixels or polygons) assigned to a certain map label as against the actual ground truth category (Congalton, 1991). Error matrix allows for the computation of descriptive accuracy statistics for the overall classification exercise (i.e. overall accuracy) but also the accuracy of individual categories either as producer

accuracy or user accuracy. Further, the error matrix serves as a basis for applying discrete multivariate analysis like KAPPA in evaluating the performance of different classification algorithms or processes (Cohen, 1960).

1.3 Challenges to Image Classification and Advances in Complex Landscapes

Among the myriad challenges to remotely sensed image classification, sensor resolution, landscape characteristics and classification procedures have been documented as important causes of classification error (Smith et al. 2002; Wu et al. 2008; Fritz et al. 2011). Despite improved spatial and spectral characteristics of satellite and aerial imaging systems, classification efforts are still challenged by a continuously evolving and complex rural and urban landscape conditions resulting from diverse land-use scenarios. Landsat images which are possibly the most widely used data source often falls short of satisfying land use and land cover classification requirements particularly in a complex rural-urban landscapes, owing to its relatively coarse spatial resolution (Lu and Weng, 2005). Alternatively, high spatial resolution images like IKONOS, Quickbird and Worldview have been promoted for land-cover classification (Sugumaran et al. 2002; van der Sande et al. 2003; Lu et al. 2010) and mapping of impervious surfaces in urban environments (Goetz et al. 2003; Lu and Weng 2009; Kamphaus 2014). Although this has been advantageous in minimizing mixed pixel problems (Lu and Weng, 2009) with relatively more detailed information extraction potential, such high resolution data are constrained by shadows, high spectral variation within the same land cover class (Lu et al. 2010; Lu and Weng 2009) and high processing requirements (Lu and Weng 2007). These disadvantages create difficulties in selection of effective classification procedures and may further result in low classification accuracies (Cushnie 1987; Lu et al. 2010).

Further, landscape characteristics such as heterogeneity have been reported to exert a direct influence on classification accuracy (Smith et al. 2002; Smith et al 2003; Lu et al. 2010). Land-cover spectral and spatial heterogeneity resulting from landscape composition are considerably different in rural and urban landscapes. For instance while rural landscapes are mainly characterized by large expanses of agricultural fields with few human settlements, urban landscapes are predominantly composed of built up surfaces such as roads, buildings, roof-tops, parking lots etc. The high variation in spectral signatures of built surfaces thus renders urban landscapes spectrally more heterogeneous (Lu et al. 2010) which may cause misclassification and ultimately reduce accuracy. Moreover sizes and shapes of built surfaces exhibits enormous variation and may lead to inaccuracies in classification (Tran et al. 2014).

In dealing with the limitations associated with coarse and medium resolution images, sub-pixel classification approaches have been developed to allow more accurate land-cover

classification especially in complex landscapes. To this end, spectral mixture analysis (SMA) and fuzzy-set classification techniques are popular approaches to deal with mixed pixel problems (Lu and Weng 2007). By allowing multiple class membership at the individual pixel level, fuzzy-set classification techniques aids in a more accurate classification and area estimation of land-cover than traditional per-pixel methods (Woodcock and Gopal 2000; Zhang and Foody 2001). SMA on the other hand models each pixel as a linear combination of individual endmember spectra (Lu and Weng 2007; Dopido et al. 2011). The output is a set fractional abundance images, with each representing one endmember spectrum. Hussin and Atmopawiro (2004) observed a higher accuracy when using sub-pixel classification (75 %) relative to maximum likelihood classification (57 %) in detecting single tree felling from 30 m Landsat ETM+ images. Similarly, other studies have demonstrated the accuracy enhancing capability of SMA in vegetation cover estimation (Sohn and McCoy 1997; Small 2001; Bai et al. 2012), burn severity mapping (Quintano et al. 2013), and land-cover mapping (Tran et al. 2014).

Per-pixel classification often results in noisy outputs due to high spatial frequency (Lu and Weng 2007; Lu et al. 2010) particularly for high resolution images in heterogeneous landscapes. Accordingly, object oriented classification approaches have been explored to minimize landscape heterogeneity effects on classification accuracy with better results (Yu et al. 2006; Mathieu and Aryal 2007; Mallinis et al. 2008; Zhou et al. 2008). Further, incorporation of textural features to spectral information has been proven to enhance classification accuracy in heterogeneous landscape conditions (Shaban and Dikshit 2001; Puissant et al. 2005; Pacifici et al. 2009). However there is a challenge in the selection of suitable texture due to its dependence on the type of image data used and the features of the landscape under study (Lu et al. 2010).

1.4 Rational of the Study

Within the study area, the rural-urban interface is extremely diverse in terms of land-use and land-cover types. Sizes and material composition of impervious surfaces changes greatly from urban to rural areas, leading to varying spectral signatures and ultimately misclassification. This creates a challenge in choosing suitable classification algorithms and image processing methods (Lu et al, 2010). The use of object-oriented approach (MacLean and Congalton 2012) and the incorporation of texture and spectral bands (Lu et al, 2010) have been explored to enhance image classification accuracy in similar contexts. Yet these studies are restricted to urban areas and little is known about the performance of classification processes when simultaneously considering rural and urban landscapes. Moreover, no prior studies reports on how classification accuracy changes along such a rural-urban gradient. Therefore a focus on

how to effectively use the features of remotely sensed data together with a suitable selection of classification approaches is vital to improve classification accuracy at the rural-urban interface, while knowledge of the distance-dependence of classification accuracy along the rural urban gradient will contribute to literature and enrich understanding of the effects of landscape characteristics on classification accuracy.

1.5 General objective

The general objective of this study is to examine the influence of spatial resolution, land cover heterogeneity and spectral un-mixing techniques on accuracy of land cover mapping at the rural-urban interface in Bangalore-India.

1.6 Specific objectives

Specifically, this study focuses on;

1. Comparing the influence of different spatial resolutions in combination with Support Vector Machines and Random Forest algorithms on accuracy of land cover mapping at the rural-urban interface
2. Evaluating the performance of spectral un-mixing for feature extraction prior to classification with Support Vector Machines at the rural-urban interface
3. Analyzing the effect of land-cover spectral and spatial heterogeneity on changes in classification accuracy along the rural-urban gradient

2. Study Area, Materials and Methods

2.1 Study Area

A 50 x 5 km transect was chosen in the northern part of Bangalore, containing different land use categories in rural, urban and suburban areas in the context of FOR2432/1 project. For the analysis of classification accuracy, the transect was divided into 5x5 km subsets (Figure 2.1).

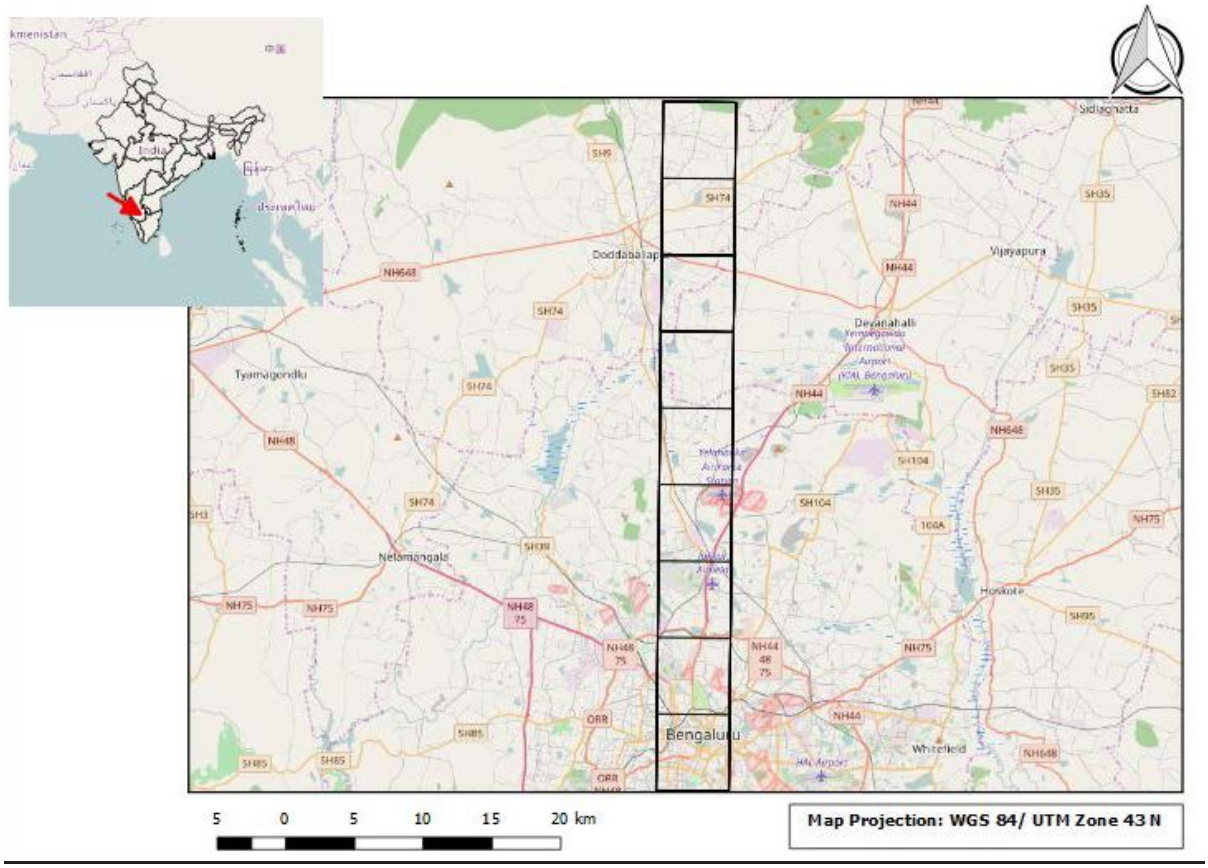

Figure 2. 1 Map of study area centered on Bangalore District - India with the 2500 km² transect and five-kilometer vertical divisions

Bangalore is located in the Indian State of Karnataka. The city is a popular center for Information Technology, Biotechnology, Aerospace and other knowledge based industries (Hiremath et al. 2013). Bangalore rural and urban districts have a geographical extent ranging between N 13°21': N 12°39' and E 77°15': E 77°51'. The area is a rapidly growing megapolis with concomitant increases in population (from 163,091 in 1901 to 8,499,399 in 2011) (Census of India 2011), economic activity and urban sprawl. This extensive growth has resulted in

landscape fragmentation and remarkable changes in land use along the rural-urban interface (Sudhira and Nagendra 2013).

2.1.1 Physiography and Climate

Bangalore lies on Southern India's Deccan plateau, at about 920 m above msl (Sudhira and Nagendra 2013). The topography is relatively flat at the Northern taluk while the Southern taluk is slightly undulating, with a central ridge running in north-east and south-west direction. The area is drained by two small rivers. River Arkavathi flows through a small stretch of Bangalore North while River Vrishabhavathi which is a tributary of Arkavathi runs through the city (BBMP 2010; Sudhira and Nagendra 2013). Further, the city and peripheral regions are dotted by a network of freshwater lakes and reservoirs (figure 2.2). According to the BBMP (2010), over 200 lakes are located within greater Bangalore.

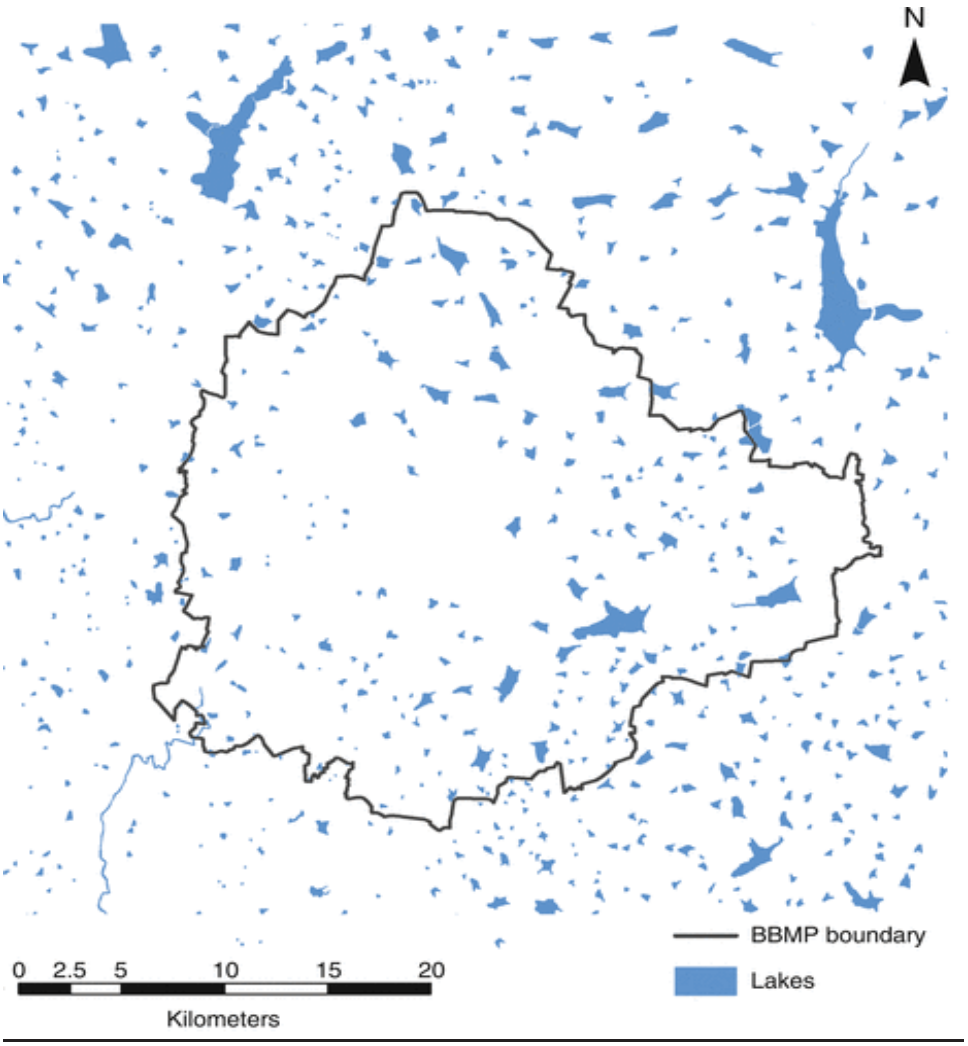

Figure 2. 2 Distribution of lakes within Bangalore and surrounding areas (Sudhira and Nagendra 2013)

Bangalore urban and rural districts lie within the tropical savanna climate zone characterized by distinct wet and dry seasons (Gayathri et al. 2013). Generally, the district experiences moderate climatic conditions throughout the year. June to September and October to November represents two windows within the rainy season and corresponds to the South-West and North-East monsoons respectively (Indian Meteorological Department 2013). Gayathri et al. (2013) reports the general annual rainfall to average around 889 mm. Mean annual minimum temperature is 15±1 ^{0}C, observed in January, whereas April is the hottest month with a mean maximum temperature of 33.6 ^{0}C (Gayathri et al. 2013,Indian Meteorological Department 2013).

2.1.2 Vegetation

A variety of green spaces occur in Bangalore rural and urban districts and varies considerably within various land use categories, including parks, wetlands, remnant forests, home gardens, wooded streets and agricultural fields (Sudha and Ravindranath 2000; Nagendra and Gopal 2011; Sudhira and Nagendra 2013). For example Sudha and Ravindranath (2000) reported high tree species richness and density in areas where land use is recreational (e.g. in parks and around lakes). However commercial and residential (i.e. high built-up areas) areas generally exhibit a low tree density. Moreover, urban areas hold a greater heterogeneity in tree species type with a high fraction of exotic species compared to rural and forested areas (Nagendra and Gopal 2011; Sudhira and Nagendra 2013). Only few patches of remnant natural vegetation exist due to anthropogenic activities, and are largely confined to rural forested areas. Streets and parks in the urban district tend to be dominated by old large canopy shade trees while recent plantings are small canopy ornamental trees (Sudhira and Nagendra 2013).

2.2 Materials

Landsat 8, Sentinel 2A and Worldview3 datasets (figure 2.3) acquired simultaneously during cloud free conditions in November 2016 were used in this study. All image datasets were received in WGS84 Universal Transverse Mercator (UTM) zone 43N projection as GeoTiFF image format. The Landsat 8 and Sentinel 2A images were processed to surface reflectance and served as the basis for land cover mapping whereas the high resolution Worldview 3 image mainly served the purpose of map validation. Table 2.1 shows a summary of source and properties of the image datasets.

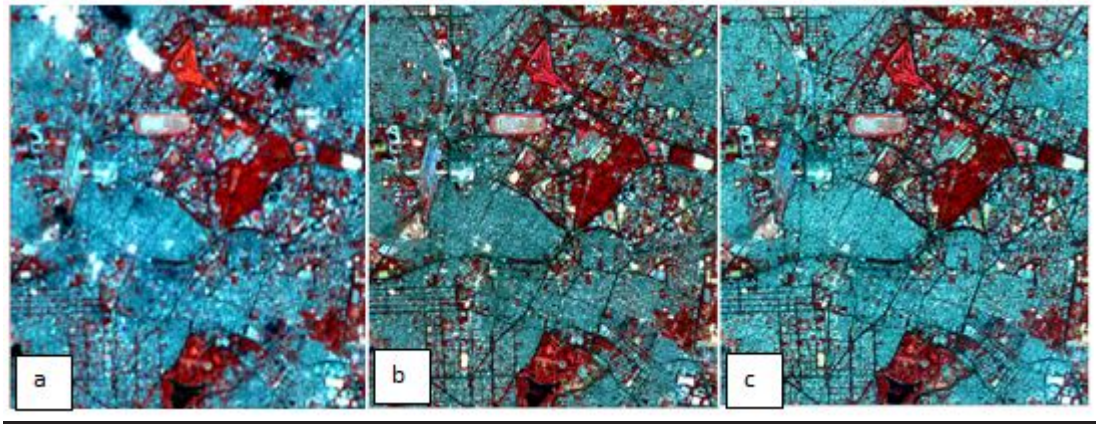

Figure 2. 3 Urban scenes of satellite images used for the study (a = Landsat 8, b = Sentinel 2A and c = World View 3)

Table 2. 1 List of satellite image data collected for the study

Satellite data	Acquisition date	Resolution	Source
Landsat 8	November, 2016	30 m Visible, Near Infrared (NIR), Short-Wave Infrared (SWIR), 100 m Thermal Infrared (TIR), 15 m panchromatic	USGS
Sentinel-2a	November, 2016	10 m, 20 m and 60 m in Visible and Near Infrared (NIR) to Short-Wave Infrared (SWIR) spectral range	European Space Agency (ESA)
Worldview-3	November, 2016	31 cm panchromatic, 1.24 m multispectral, 3.7 m Short-Wave Infrared (SWIR), 30 m Clouds, Aerosols, Vapors, Ice, and Snow (CAVIS)	Digital Globe Inc.

2.3 Methods

2.3.1 Classification Scheme

Within the study area a mixture of different land uses ranging from agricultural to industrial can be identified. Consequently the area is characterized by a broad spectrum of anthropogenic (e.g. concrete, asphalt, metals, roofing material etc.), semi-natural (e.g. grass, fields, reservoirs) and natural (e.g. lakes, trees, bare soil) land cover features. A classification scheme for land cover categories encountered was thus developed such that as much spatial and spectral heterogeneity as possible was covered along the gradient. Overall, eight classes were finalized, namely; built-up, tree cover, grassland, reservoir, lake, barren land, fallow land and crop fields (see table 2.2).

2.3.2 Training Strategy

Due to the varying composition of land use and land cover types within the study area, the transect was analyzed and vertically differentiated into urban, suburban and rural regions based on the degree of urbanness to aid the collection of training samples that span the inherent spectral variability in land cover classes. Further, this fed into a semi-variance analysis used to assist the collection of non-correlated training samples.

2.3.2.1 Determining Urban, Suburban and Rural extents

A preliminary supervised classification of Landsat 8 imagery was conducted for the purpose of determining the degree of urbanness along the gradient. Although aspects of the social environment are largely employed in defining urban environments, assessment of composition and configuration of all pixels within a defined geographic region has been identified as a useful consideration in developing indices that measure urban extents (Rashed and Jürgens 2010). Of principal interest is the observation of changes in the built-up environment. Hence, the extent of urban, suburban and rural areas was based on the composition of pixels in the classified Landsat 8 imagery. Using a fourteen by one grid (3.2 km^2) and a cross-classification approach, the gradient was differentiated into urban, suburban and rural depending on the share of built up pixel found within the grid.

Table 2. 2 Land cover classification scheme

Class number	Class name	Description
Class 1	Built-up	Structures with walls and roof, including residential buildings, industrial buildings etc, long surfaced vehicle tracks, mostly asphalt coated, also including narrow streets and all railroad systems, predominantly metallic tracks
Class 2	Tree cover	Patches of leaved trees within the landscape
Class 3	Grassland	Areas such as urban parks and lawns but also grass-covered areas around agricultural fields
Class 4	Reservoir	Man-made tanks filled with water, close to agricultural fields and often with high sediment load
Class 5	Lake	Large water bodies surrounded by land
Class 6	Barren land	Open areas covered by bare soil. Outside agricultural land use contexts
Class 7	Fallow land	Agricultural lands currently without crops
Class 8	Crop field	Agricultural lands currently covered with crops

2.3.2.2 Semi-variance for Detecting Spatial Autocorrelation

Key among the considerations for selecting training samples is spatial autocorrealation. Computation of spatial autocorrelation gives an idea about the distance at which values from different sampling points are similar. Accordingly, it is important to quantify the degree of autocorrelation to guide the selection of uncorrelated data (Chen and Stow 2002). A common method to depict the spatial characteristics of image pixels is semi-variance analysis (De Smith et al. 2007; Chen and Stow 2002). Semi-variance measures the average squared difference between pairs of values separated by a distance and has the general form:

$$\gamma(h) = \frac{\sum_{i=1}^{n}(z(i)-z(i+h))^2}{2n} \qquad \text{(Eq. 1)}$$

Where *h* is the lag or fixed distance between pixel values (*z*) at points (*i*) and (*i+h*), and *n* is the number of pixel pairs. Sill and range are common characteristics that describe a semivariogram model. The semi-variance increases gradually with distance and levels-off at a point. This point is known as the sill and the distance at which the sill is reached is called the range (De Smith et al 2007). The range signifies the distance at which spatial autocorrelation of pixel pairs ceases.

Semi-variograms for the urban, suburban and rural extents were generated using **gstat** Package in R (R Core Team 2016). The range parameters of the semi-variograms were determined by means of spherical and exponential model-fits, and the average range parameter from the model with the best fit was utilized in the collection of training data (Chen and Stow 2002).

2.3.2.3 Sampling

A systematic sampling approach was adopted for the collection of training data. Here, more emphasis was placed on obtaining samples large enough with adequate spatial distribution. This was to ensure that both rare and frequently encountered land cover types were well sampled to cover all spectral variability within classes (Foody and Mathur 2004).

Using the MMQGIS plugin available in QGIS (QGIS Development Team 2017), a 140 point grid layer was created to cover the whole extent of the image subsets. However, only 78 points came to lei completely within the extent of the imagery. The average range parameter derived from fitted semi-variograms for the rural, suburban and urban extents of Landsat 8 image subset was utilized as point spacing for the systematic point grid. Hence spatially auto-correlated samples were avoided. Circular polygon buffers of 500 m radius were installed at each sampling point to serve as response units within which training samples were recorded.

The number of training samples was determined by means of simple heuristics which gives sample size as a function of image data dimensionality (Foody et al. 2006; Mather 1999). Mather (1999) recommends using a minimum of 10*p* to 30*p* training pixels for each thematic class, where *p* is the number of spectral bands used. Thus with a minimum and maximum of seven (Landsat 8) and ten (Sentinel 2A) spectral bands respectively used in this study, the minimum required training pixels per class lies between 70 and 100. Using eight thematic classes, a total of 560 to 800 training pixels were needed for the whole classification. Nonetheless 809 polygons of pixels (i.e. approximately, Landsat 8 = 12,294 training pixels and Sentinel 2A = 122,940 training Pixels) were used in this study, which is considerably above the minimum recommended by Mather (1999).

2.3.2.4 Class Training

The underlying feature of supervised land cover classification is class training. Training set for defined land cover classes (Table 2.2) were selected by visually identifying and digitizing polygons of pixels within the response units (Chen and Stow 2002) rather than individual pixels. As noted by McCoy (2005) and Momeni et al. (2016), using polygons or blocks of pixels as training units can prevent the selection of potentially noisy individual pixels. In essence several polygons were selected for each land cover class to adequately characterize their spatial and spectral properties. The same polygon extents and locations were used to extract training samples at the different spatial resolutions in order to allow a direct comparability of results. Class training for all classifiers at the different spatial resolutions was executed using Orfeo Toolbox (Image analysis) available in QGIS (QGIS Development Team 2017).

2.3.2.5 Assessment of Training Class Spectral Separability

During class training, every attempt was made to ensure spectral separability of training classes. Specifically, spectral plots of training classes were reviewed and repeatedly modified until all class training sets attained adequate spectral separability. Further, the Jefferies-Matusita (JM) distances for pairs of class training sets were computed to provide a statistical evaluation of training class separability. The JM distance is a commonly used measure for defining spectral (dis)similarity of thematic classes (Van Niel et al. 2005; Dabboor et al. 2014; Momeni et al. 2016). A major component of the JM separability measure is Bhattacharyya (*B*) distance calculated as (Van Niel et al. 2005):

$$B = \frac{1}{8} D^2_{\text{pool}} + \frac{1}{2} \ln \frac{\left| \frac{\Sigma_i + \Sigma_j}{2} \right|}{\sqrt{|\Sigma_i| * |\Sigma_j|}} \qquad \text{(Eq. 2)}$$

Where D^2_{pool} is the pooled Malanobis distance for classes *i* and *j*, and ∑ is the variance-covariance matrix (Van Niel et al. 2005). The pooled Malanobis distance is calculated as:

$$D^2_{pool} = (\mu_i - \mu_j)^T \left(\frac{\Sigma_i + \Sigma_j}{2} \right) (\mu_i - \mu_j) \qquad \text{(Eq. 3)}$$

Where μ_i and μ_j are the mean reflectance values for classes *i* and *j* (Van Niel et al. 2005). Hence the JM separability measure between two classes is computed as:

$$JM = 2(1 - e^{-B}) \qquad \text{(Eq. 4)}$$

The JM distance asymptotically approaches 2 when the class spectral signatures are completely different and falls to 0 when spectral signatures are identical (Richards and Jia

2006). For JM values below 1.3, training classes were refined and in some cases merged until all classes were satisfactorily separable.

2.3.3 Feature Extraction

2.3.3.1 Spectral Unmixing

In cases where the spatial resolution of sensors are not fine enough to record pure signals from surface materials, multiple signals from different materials can occupy a single pixel. As such, the reflectance per pixel is assumed to be the result of a linear combination of the reflectance of each constituent material within the pixel (Dopido et al. 2011). Consequently, spectral un-mixing is an approach to decompose the measured spectrum from a mixed pixel into constituent endmembers and a collection of fractional abundances indicating the proportion of each endmember within the pixel (Keshava and Mustard 2002). Here linear spectral un-mixing and partial un-mixing techniques for feature extraction were applied to Landsat 8 and Sentinel 2A scenes. Using the linear mixture model, each pixel X (where X = $[x_1,\ldots,x_n]$ for n band remotely sensed scene) can be modeled as (Dopido et al. 2011)

$$X = \sum_{z=1}^{p} \varphi_z \cdot E_z + n \qquad \text{(Eq. 5)}$$

Where p is the number of endmembers, n is a noise vector, E_z is the spectral response of endmember z and φ_z is its fractional abundance. Two constraints can be considered under the linear mixture model, namely: the abundance sum-to-one constraint ($\sum_{z=1}^{p} \varphi_z = 1$) and abundance non-negative constraint ($\varphi_z \geq 0$) (Dopido et al. 2011).

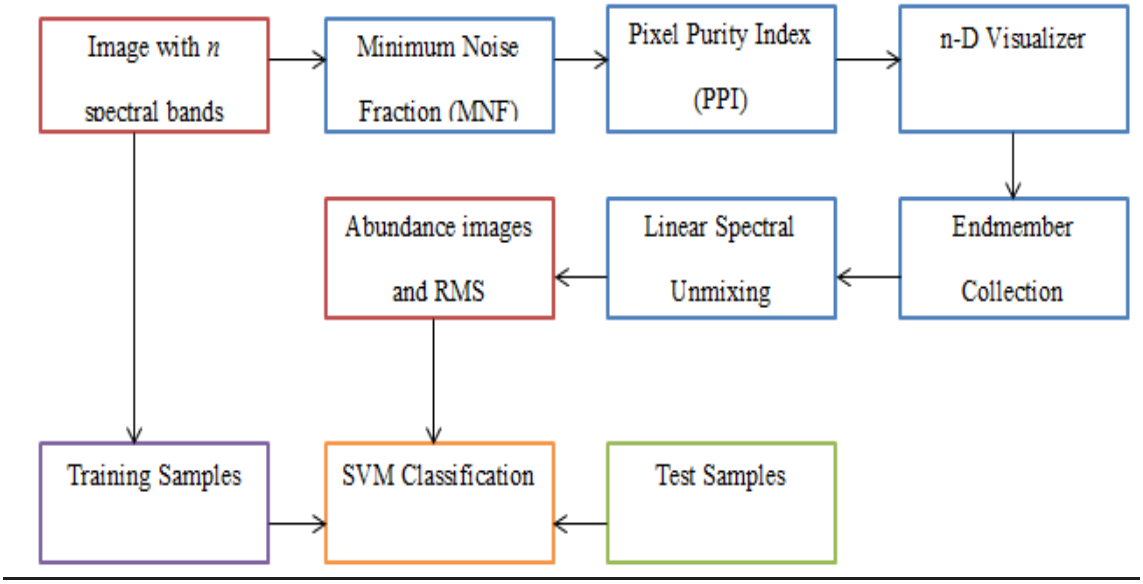

Figure 2. 4 Steps for spectral un-mixing sequence 1

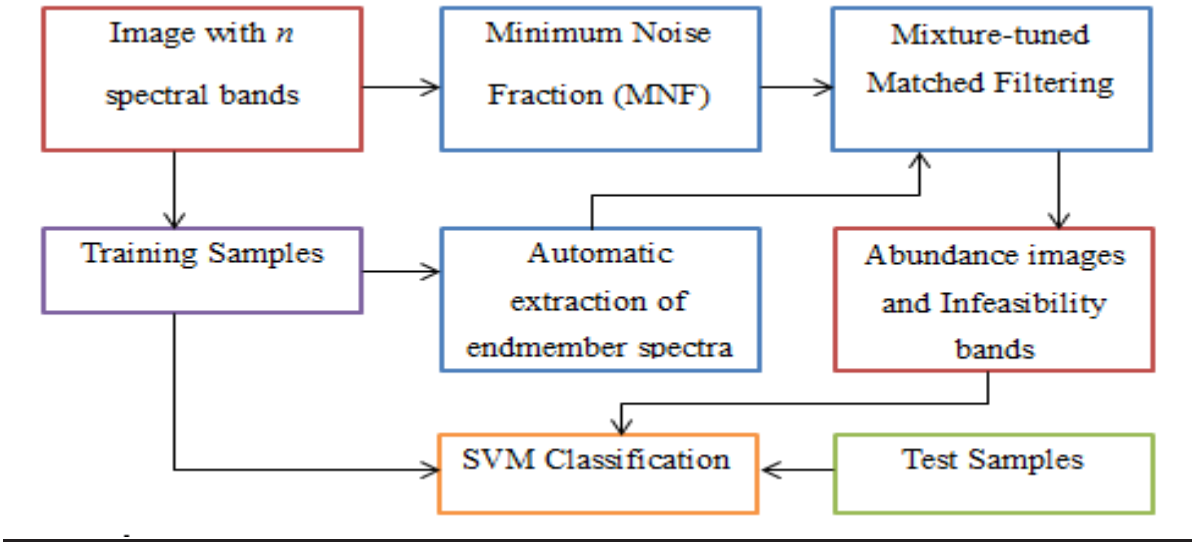

Figure 2. 5 Steps for spectral un-mixing sequence 2

Unmixing Sequence 1

The first sequence of spectral un-mixing based feature extraction is summarized in figure 2.4. First, Minimum Noise Fraction rotation transform was applied to the original image data to check the inherent dimensionality and to select less noisy bands for further processing based on their eigenvalues. Next, the Pixel Purity Index was run on the output from MNF

transformation to highlight pure pixels. The PPI is a standard technique to determine the most spectrally pure pixels in remotely sensed images (Liming et al. 2012). The output pure endmembers from the PPI were then extracted into the n-D Visualizer in ENVI to examine and refine endmember spectra for Linear Spectral Un-mixing. In effect, Linear Spectral Un-mixing with a sum-to-unity constraint was applied to estimate the abundance of each derived endmember. Finally, a supervised classification using Support Vector Machine (SVM) was executed on the abundance fractions.

Unmixing Sequence 2

Due to the challenge of estimating the number of endmembers from the original image and accompanying computation complexity (Plaza et al. 2009), a variation of the first un-mixing sequence was developed and implemented. Figure 2.5 summarizes the second un-mixing sequence where endmember spectra were collected from the labeled training samples as an alternative to endmember extraction from the original image data. This minimizes computational tasks since endmember extraction is conducted only on the training samples. Moreover, since the number of extracted endmembers is defined according to the different training classes, the challenge of estimating the number of endmembers becomes simplified. Nonetheless, the actual number of endmembers could be more in the original image data than the labeled training classes. Therefore the Mixture-Tuned Match Filtering (MTMF) technique was used to partially un-mix the original image data with MNF transformed results as input data. The MTMF process integrates Linear Spectral Un-mixing and statistical match filtering (Dopido et al. 2011). Thus it leverages the capability to return endmember abundance fractions from spectral mixture modeling, and reduction in the number of false positives arising from match filtering by adding infeasibility image bands. Following the MTMF process, a supervised classification was performed on the abundance fractions using SVM classifier.

2.3.3.2 Principal Component Analysis (PCA) and Noise Adjusted Principal Component Analysis

Feature extraction techniques that are able to enhance the performance of SVM classification by reducing image data dimensionality while preserving the original information (Melgani and Bruzzone 2004; Plaza et al. 2009; Dopido et al. 2011) were applied to Landsat 8 and Sentinel 2A scenes in order to evaluate the performance of spectral un-mixing for feature extraction. Here Principal Component Analysis (PCA) and Noise Adjusted Principal Component (NAPCA) transformation techniques were used. The PCA transform thrives on the maximization of data variance to yield new uncorrelated dataset while the NAPCA maximizes signal-to-noise ratio (SNR). Both PCA and NAPCA transformations was executed using Orfeo-Toolbox available in QGIS (QGIS Development Team 2017).

2.3.4 Image classification

Pixel-based classification was performed using two supervised non-parametric classifiers namely, Support Vector Machine and Random Forest.

The selection of non-parametric classification approaches was contingent on their special ability to handle complex classification problems. For example, when using fine spatial resolution imagery, alongside a detailed classification scheme to map heterogeneous environments (Momeni et al. 2016). In this context, the inherent spatial heterogeneity in high (Sentinel 2A) and medium (Landsat 8) resolution imagery used, high spectral variation within land cover classes and the training strategy adopted renders them more suitable compared with parametric methods.

2.3.4.1 Support Vector Machine (SVM)

The support vector machine classifier is a non-parametric binary learning algorithm based on statistical learning theory (Vapnik 2013). SVMs have increasingly been applied in image classification, often yielding high accuracies over other conventional methods (Hamedianfar et al. 2014; Foody et al. 2006; Nong et al. 2015). The algorithm seeks to generate an optimal separating hyper-plane between two classes by setting decision boundaries using the location of training samples at the edges of class distributions (Belousov et al. 2002; Marjanovic et al. 2011). These samples represent support vectors while all other training samples are effectively excluded from the learning process (Foody et al. 2006). The classification function is given by (Marjanovic et al. 2011),

f (x) = sign $(\sum_{i=1}^{n} \alpha_i y_i (x_i \cdot x) + b)$ (Eq. 6)

In order to handle non-linearity of classification problem, the initial space is mapped to a higher dimension feature space using non-linear functions ($\emptyset$). This allows a transformation of the non-linear case in a manner that aids the definition of a linear hyper-plane (Borges et al. 2004). Kernel functions (given by k(x,y) = $\emptyset(x) \cdot \emptyset(y)$) such as polynomial kernels and radial basis function are used for this transformation (Borges et al. 2004; Marjanovic et al. 2011). Using these functions equation 5 becomes

f (x) = sign $(\sum_{i=1}^{n} \alpha_i y_i k(x_i \cdot x) + b)$ (Eq. 7)

The SVM classification was implemented using Orfeo Toolbox (Image analysis) available in QGIS (QGIS Development Team 2017). Here the Radial Basis Function (Gaussian RBF) kernel type was used because it addresses non-linear problems and is popular for practical use

(Keerthi and Lin 2003). The cost parameter (C) and gamma for the kernel were set at 500 and 1 respectively. The parameter settings were made with consideration to prevailing literature (Momeni et al. 2016) and some heuristics.

2.3.4.2 Random Forest (RF)

The Random Forest classifier is an ensemble learning algorithm which presents many advantages for remote sensing applications (Rodriguez-Galianon et al. 2012). The algorithm assigns input vectors (independent and identically distributed random vectors) to the most frequent classes based on single vote contributions from each classifier within the ensemble (classification trees) (Breiman 2001). Individual classification trees making up the algorithm are grown from different subsets of training data selected through bootstrap aggregation or bagging, while using the Gini index as a measure for attribute selection (Pal 2005). Thus for a particular training set (*T*), assigning pixels selected at random to a class (C_i) expresses the Gini index as:

$\sum\sum_{j \neq i} (f(C_i, T)/|T|) \cdot (f(C_j, T)/|T|)$ (Eq. 8)

Where $f(C_i, T)/|T|$ is the probability that the selected case belongs to class C_i (Pal 2005; Rodriguez-Galianon et al. 2012).

The number of classification trees and the number of samples used in each node are the two parameters that must be defined to create a prediction model. Here, default values of 100 trees and 10 samples in each node were selected for implementation. The RF classification was implemented using Orfeo Toolbox (Image analysis) available in QGIS (QGIS Development Team 2017).

2.3.5 Validation and Accuracy Assessment

A common validation and accuracy assessment approach was adopted for all land cover classification outputs in order to allow a direct comparison of classification methods at the different spatial resolutions. An independent validation data was collected using very high resolution WorldView 3 scene as reference image. A dense point-based checking was employed and land cover classes beneath these points were recorded by visual interpretation in conformity with the classification scheme. Further, field visits were undertaken between April 18, 2017 and May 2, 2017 to ascertain the veracity of validation datasets. The same point locations were used for all classified map outputs, thus ensuring that results were directly comparable. Accuracy assessment of the six output land cover maps was implemented using

the Semi-automatic Classification Plugin (SCP) available in QGIS (QGIS Development Team 2017).

The error matrix has been recommended as a standard approach to represent map accuracy (Congalton 1991; Foody 2002). Thus error matrices were generated to elicit the correspondence between reference data and classification output, allowing for the computation of individual class accuracies (i.e. user's accuracy and producer's accuracy), overall map accuracy and Kappa statistic. A mathematical representation of the error matrix and calculation of these accuracy measures are illustrated herewith. Assuming each pixel to be classified belongs to one of four mutually exclusively defined classes (*k*), let $n_{i\ j}$ represent the number of pixels classified into category *i* in the classification output (i.e. rows, where *i* = A, B, C, D) and independently to category *j* in the reference dataset (i.e. columns, where *j* = A, B, C, D) (see table 3.4).

Table 2. 3 Error matrix for classification accuracy assessment (after Congalton 1991)

	A	B	C	D	Total ($n_{i\ +}$)
A	$n_{A\ A}$	$n_{A\ B}$	$n_{A\ C}$	$n_{A\ D}$	$n_{A\ +}$
B	$n_{B\ A}$	$n_{B\ B}$	$n_{B\ C}$	$n_{B\ D}$	$n_{B\ +}$
C	$n_{C\ A}$	$n_{C\ B}$	$n_{C\ C}$	$n_{C\ D}$	$n_{C\ +}$
D	$n_{D\ A}$	$n_{D\ B}$	$n_{D\ C}$	$n_{D\ D}$	$n_{D\ +}$
Total ($n_{+\ j}$)	$n_{+\ A}$	$n_{+\ B}$	$n_{+\ C}$	$n_{+\ D}$	n

Overall accuracy can be calculated as: OA = $\frac{\sum_{i=1}^{k} n_{i\,i}}{n}$ (Eq. 9)

Producer's accuracy can be calculated as: PA = $\frac{n_{i\,i}}{n_{i+}}$ (Eq. 10)

User's accuracy can be computed as: UA = $\frac{n_{j\,j}}{n_{+\,j}}$ (Eq. 11)

Kappa statistic can be calculated as: K = $\frac{n\sum_{i=1}^{k} n_{i\,i} - \sum_{i=1}^{k} n_{i+}n_{+\,j}}{n^2 - \sum_{i=1}^{k} n_{i+}n_{+\,j}}$ (Eq. 12)

Comparison of classification methods is an integral component of this study. Therefore a rigorous approach for testing the statistical significance of differences in classification outputs was adopted. Here the two sample z test was performed on all pairs of Kappa values for land cover maps (Foody 2004; Foody et al. 2006). The z test is the standard normal statistic (z) and is calculated as:

$$z = \frac{K_i - K_j}{\sqrt{\frac{\sigma^2 K_i}{n} + \frac{\sigma^2 K_j}{n}}} \quad \text{(Eq. 13)}$$

Where K_i represents Kappa value for land cover map *i,* K_j represents Kappa value for land cover map *j,* σ^2 is standard deviation of Kappa coefficient and *n* is the number of samples. The standard deviation of Kappa coefficient is calculated as (Cohen 1960):

$$\sigma^2{}_K = \sqrt{\frac{OA(1-OA)}{(1-EA)^2}} \quad \text{(Eq. 14)}$$

Where *OA* is the observed accuracy and *EA* is the expected accuracy.

2.3.6 Gradient Analyses

A simple vertical differentiation approach was adopted to analyze the distance-dependence of classification accuracy along the urban-rural gradient. Here, multiple extents of the whole urban-rural transect was generated at five kilometers interval from the urban to rural region. The five-kilometer vertical zonation was arbitrarily defined. Even so, this ensured a uniform segregation of the rural-urban transect. Further, the analysis was augmented by the spectral variability assessment conducted within the each of the five kilometers extents along the urban-rural gradient to reinforce understanding of changes in classification accuracy.

2.3.7 Land-cover heterogeneity assessment

2.3.7.1 Assessment of land-cover spectral variability

An assessment of spectral variation was conducted to aid the interpretation and evaluation of classification results along the gradient. Thus the spectral characteristics of land cover types within each five kilometers distance was evaluated to identify the spectral complexity of surface materials along the urban-rural gradient using ENVI 5.1 (Exelis Visual Information Solutions 2014). The process is summarized in figure 2.6.

An automated endmember extraction approach using the Sequential Maximum Angle Convex Cone algorithm (SMACC) (Gruninger et al. 2004) was adopted. Thus endmember spectra from Sentinel 2A scenes were collected along the urban-rural gradient. Extracted endmembers were visually identified from high resolution WorldView 3 scene and grouped according to their corresponding land surface material. Lastly, the spectral separability of extracted endmembers belonging to the same land cover type was computed using Jefferies-Matusita distance.

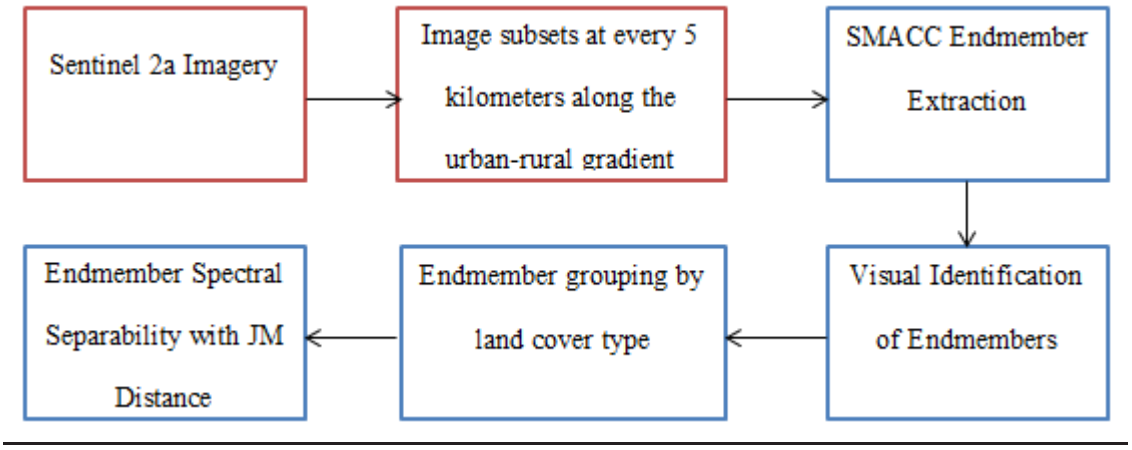

Figure 2. 6 Steps for spectral variability assessment

2.3.7.2 Assessment of land-cover spatial variability

The spectral variability assessment along the gradient was further augmented by quantifying the spatial composition and configuration of the rural-urban landscape. Thus four landscape metrics were selected and calculated using Fragstats- a spatial analyst program for categorical maps (McGarigal and Marks 1995). The selected landscape metrics were Patch Density (PD), Landscape Shape Index (LSI), Contagion Index (CONTAG) and Shannon's Diversity Index (SHDI).

The PD, LSI and CONTAG metrics quantifies the spatial configuration of all land cover types within the rural-urban landscape while SHDI provides information on landscape composition.

Patch Density (PD) provides a general perspective of spatial heterogeneity of an entire landscape (McGarigal et al. 2002) and is calculated as:

$$PD = \frac{N}{A}\ (10{,}000)(100), \qquad \text{(Eq. 15)}$$

where *N* is the number of patches in the landscape and *A* is the total landscape area. The Patch Density of a landscape is expressed as the number of patches per 100 hectares.

Landscape Shape Index (LSI) is an expression of the configuration of a landscape in terms of the extent of edges present in the landscape compared to a completely compact landscape of the same size with a squared shape (McGarigal et al. 2002). The LSI increases with an increasing edge length within the landscape and is expressed as:

$$LSI = \frac{E}{\min E}, \qquad \text{(Eq. 16)}$$

where *E* is the total length of edge and *min E* is the minimum total length of edge in the landscape (McGarigal et al. 2002).

Contagion Index (CONTAG) is based on raster cell adjacencies and indicates the overall clumpiness within a landscape (McGarigal et al. 2002). CONTAG is inversely related to LSI and ranges between 0 and 100, signifying maximally disaggregated patches and maximally aggregated patches within a landscape respectively. CONTAG is given by:

$$CONTAG = 1 + \left[\frac{\sum_{i=1}^{m}\sum_{k=1}^{m}\left[(P_i)\left[\frac{g_{ik}}{\sum_{k=1}^{m} g_{ik}}\right]\right] * \left[in\ (P_i)\left[\frac{g_{ik}}{\sum_{k=1}^{m} g_{ik}}\right]\right]}{2\ln(m)}\right] * 100 \qquad \text{(Eq. 17)}$$

where P_i is landscape proportion occupied by patch type *i*, *m* is number of patches in the landscape and g_{ik} represents the number of adjacencies between pixels of *i* and *k* patch types (McGarigal et al. 2002).

Shannon's Diversity Index (SHDI) is meaningful as a relative index and quantifies the amount of information (i.e. in this case, in terms of patches) present in a given landscape (Shannon and Weaver 1949). The SHDI is given by:

$$\text{SHDI} = -\sum_{i=1}^{m}(P_i * lnP_i) \qquad \text{(Eq. 18)}$$

where P_i is landscape proportion occupied by patch type *i* and *m* is number of patches in the landscape.

3. Results

3.1 Training Data Collection

3.1.1 Urban, Suburban and Rural Areas

The regional differentiation is shown in Figure 3.1. From Table 3.1, areas with more than 50 % built-up pixels were classified as urban whereas areas with 10-50 % and 0-10 % built-up pixels were defined as suburban and rural regions respectively (Angel et al. 2012).

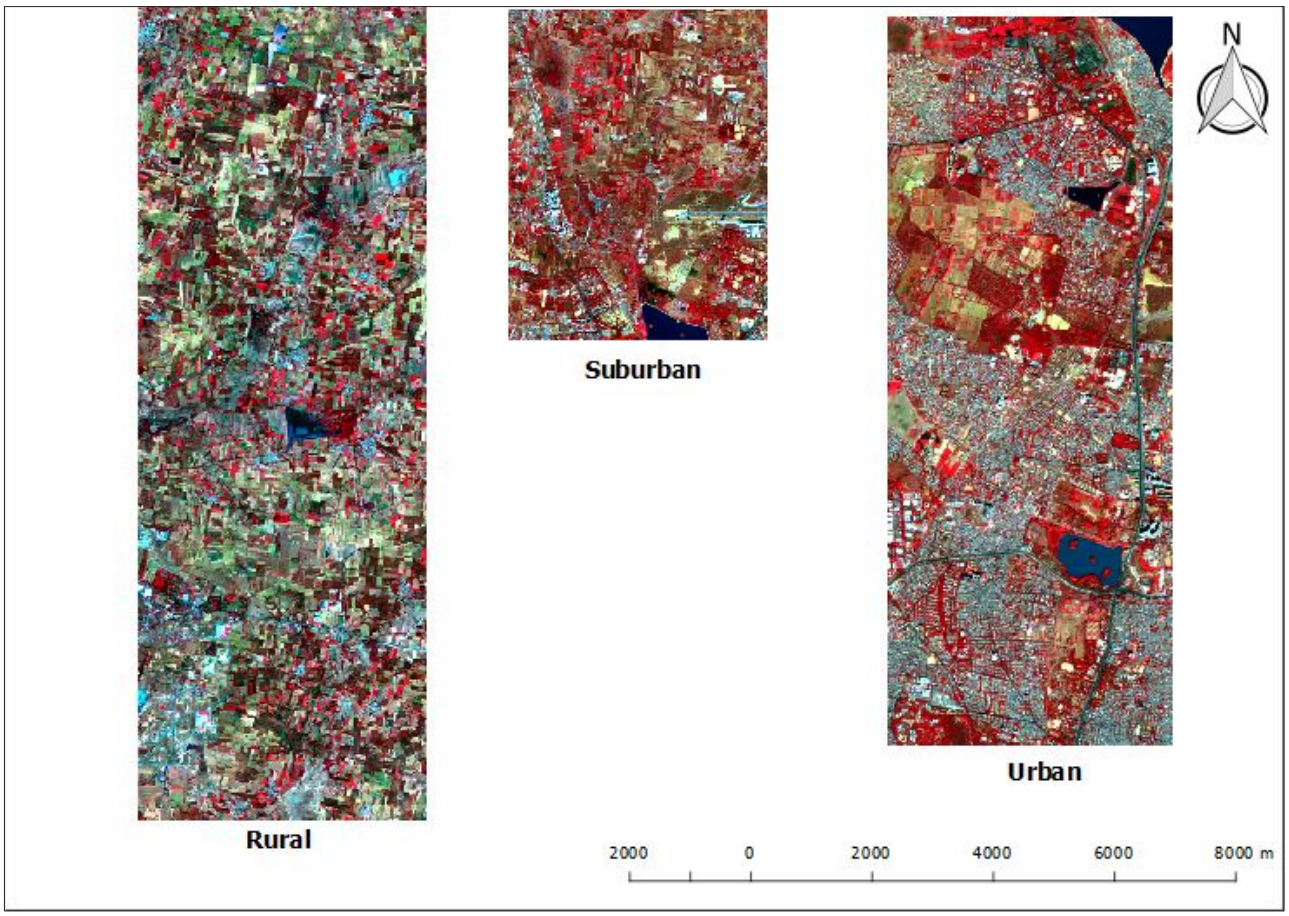

Figure 3. 1 False color composite of urban, suburban and rural regions from Sentinel 2A scene

Overall, a greater proportion of the transect (48 % = 120 km^2) was defined as rural while 14 % (45 km^2) and 38 % (95 km^2) were suburban and urban respectively. The rural region is predominantly composed of agricultural land use with patches of tree cover and a few

scattered human settlements. The suburban region represents a transition between rural and urban regions with almost even share of built-up areas and agricultural lands. Unlike the rural and suburban regions, the urban region is largely composed of heavily built-up areas interspersed with patches of tree cover (urban green) and lakes scattered from the north to south.

Table 3. 1 Cross-matrix of systematic grid cells and thematic classes showing relative proportions of class pixels based on Landsat 8 image

THEMATIC CLASSES	RELATIVE PROPORTION OF PIXELS (%)													
	a	b	c	d	e	f	g	h	i	j	k	l	m	n
Built-up	0.03	0.01	0.02	0.05	0.01	0.02	0.05	0.11	0.30	0.49	0.64	0.62	0.60	0.87
Water	0.00	0.00	0.02	0.00	0.00	0.00	0.01	0.00	0.12	0.04	0.02	0.00	0.01	0.00
Agriculture	0.85	0.86	0.82	0.78	0.79	0.65	0.58	0.36	0.15	0.15	0.16	0.12	0.11	0.02
Tree cover	0.01	0.04	0.09	0.07	0.09	0.14	0.17	0.18	0.20	0.23	0.15	0.25	0.27	0.11
Other	0.11	0.08	0.05	0.10	0.11	0.19	0.19	0.35	0.23	0.09	0.03	0.01	0.00	0.00

Labels 'a' to 'n' denote systematic grid cells from rural to urban area shown in Appendix III.

3.1.2 Semi-variance Analysis

Semi-variograms from the NIR band of Landsat 8 scene were derived separately for each regional subdivision (urban, suburban and rural: Figure 3.2) considering the apparent spatial and spectral variation along the urban-rural gradient. This was aimed at avoiding spatially auto-correlated samples for class training. Accordingly, the range parameters from the exponential variogram model-fit (Table 3.2) were implemented in the collection of training samples. It is assumed that using a range parameter derived from the coarser resolution imagery (Landsat 8) would effectively prevent auto-correlated samples across the finer resolution scenes (Sentinel 2A) due to the larger distance between pixel values.

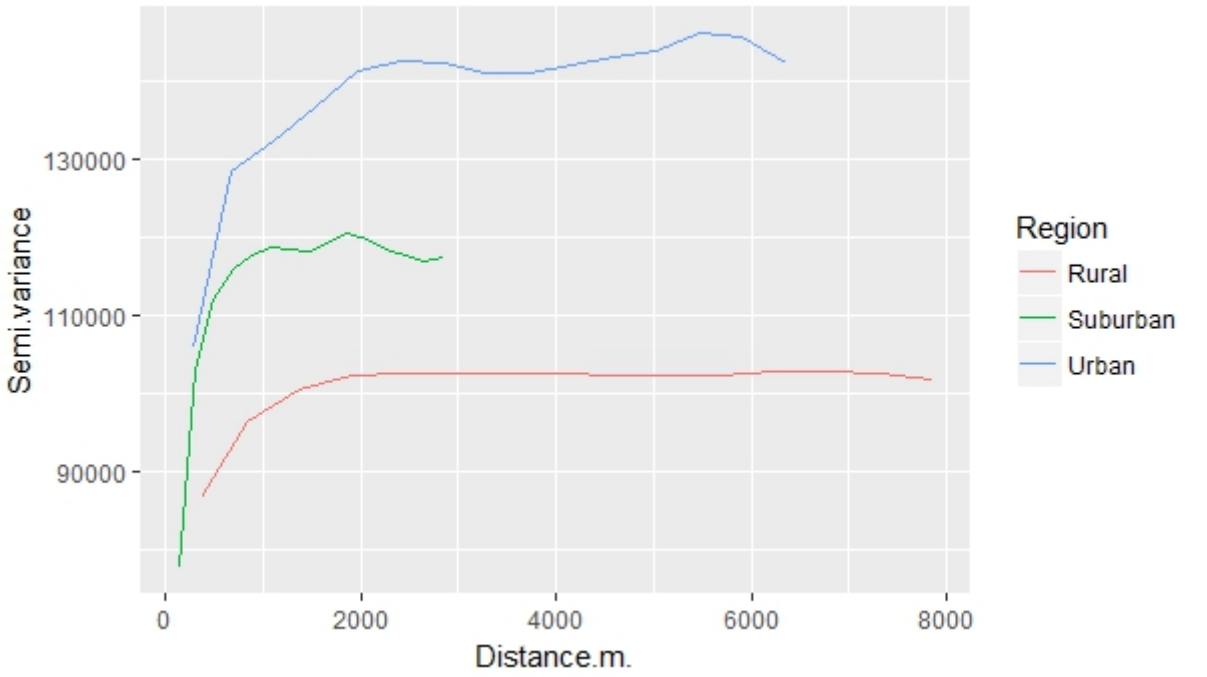

Figure 3. 2 Semi-variograms calculated from NIR band of Landsat 8 scene for urban, suburban and rural regions

Figure 3.2 shows that semi-variances increase with increasing spatial lag or distance. The semi-variograms reaches the sill more rapidly in the suburban region followed by the urban region, whereas in the rural region the sill is reached at a higher range (Table 3.2). Further, a comparison of the slopes of semi-variograms at various distances for the different regions shows the relative degrees of auto-correlation of pixel values, decreasing from rural to the urban region. Semi-variance for all regions increases rapidly at smaller distances, even so, as the lag distance increases the rate at which semi-variance increases is gradually reduced.

Table 3. 2 Semi-variogram parameters from exponential model-fit for urban, suburban and rural regions

Region	Sill	Range	Kappa
Urban	122220.1	2116.233	0.5
Suburban	97533.44	948.7916	0.5
Rural	94517.51	2619.741	0.5

3.1.3 Class Training

A total of 11,273 and 105,900 training pixels from 809 polygons were collected for Landsat 8 and Sentinel 2A images respectively (Table 3.3). Mather (1999) recommended a minimum of 10*p* training pixels for each land-cover class, where *p* represents the number of image spectral bands. This translates to a minimum of 70 pixels and 100 pixels per thematic class for Landsat 8 and Sentinel 2A data respectively. The training samples collected for each thematic class in the Sentinel 2A image were considerably larger than the minimum recommended. However, only 30 training pixels were collected for Reservoir class from Landsat 8 image data. This is largely because only single pixels could be collected, for the large Landsat 8 pixel size.

Table 3. 3 Number of training pixels for each class at 30 m and 10 m resolution

THEMATIC CLASS	NUMBER OF TRAINING PIXELS	
	Landsat 8	**Sentinel 2A**
Built-up	1899	19934
Tree cover	835	7308
Grassland	75	746
Reservoir	30	347
Lake	1827	16249
Fallowland	4281	39585
Cropfield	1782	16522
Barren land	544	5209

3.1.4 Training Class Spectral Separability

Jeffries-Matusita (JM) distance was used to quantify the degree of spectral discrimination between training samples of the different land-cover types. The separability scores for the different resolution images are presented as a matrix in Table 3.4. The JM distances generally

highlight a high degree of spectral separability. Nonetheless, low separability thresholds (highlighted in Table 3.4) were observed between Cropfields and Fallowland for both Landsat 8 and Sentinel 2A data and between Cropfields and Grassland for Sentinel 2A training data. Additionally, Barren land and Fallowland in Sentinel 2A training samples had a low separability score.

Table 3. 4 Matrix of JM distance values for spectral separability between training samples of different land-cover classes (2= complete dissimilarity, 0= complete similarity)

LANDSAT 8							
	Built-up	**Tree cover**	**Grassland**	**Reservoir**	**Lake**	**Fallowland**	**Cropfield**
Tree cover	1.99						
Grassland	1.98	1.79					
Reservoir	1.91	1.99	1.99				
Lake	1.99	1.99	1.99	1.89			
Fallowland	1.93	1.96	1.81	1.87	1.99		
Cropfield	1.96	1.83	1.88	1.83	1.99	**1.47**	
Barren-land	1.71	1.96	1.89	1.97	1.99	1.63	1.96
SENTINEL 2A							
	Built-up	**Tree cover**	**Grassland**	**Reservoir**	**Lake**	**Fallowland**	**Cropfield**
Tree cover	1.99						
Grassland	1.98	1.88					
Reservoir	1.99	1.99	1.99				
Lake	1.99	1.99	1.99	1.99			
Fallowland	1.95	1.99	1.75	1.99	1.99		
Cropfield	1.99	1.69	**1.08**	1.99	1.99	**1.49**	
Barrenland	1.95	1.99	1.98	1.99	1.99	**1.34**	1.95

3.2 Classification Results

Results of thematic land-cover classification from the different feature extraction strategies at the rural-urban interface are shown in figure 3.3 and 3.4 for Lansat 8 and Sentinel 2A images respectively. Noticeable differences can be observed in the outputs of land-cover classification with reference to raw image scenes, particularly for the lower resolution Landsat 8 maps.

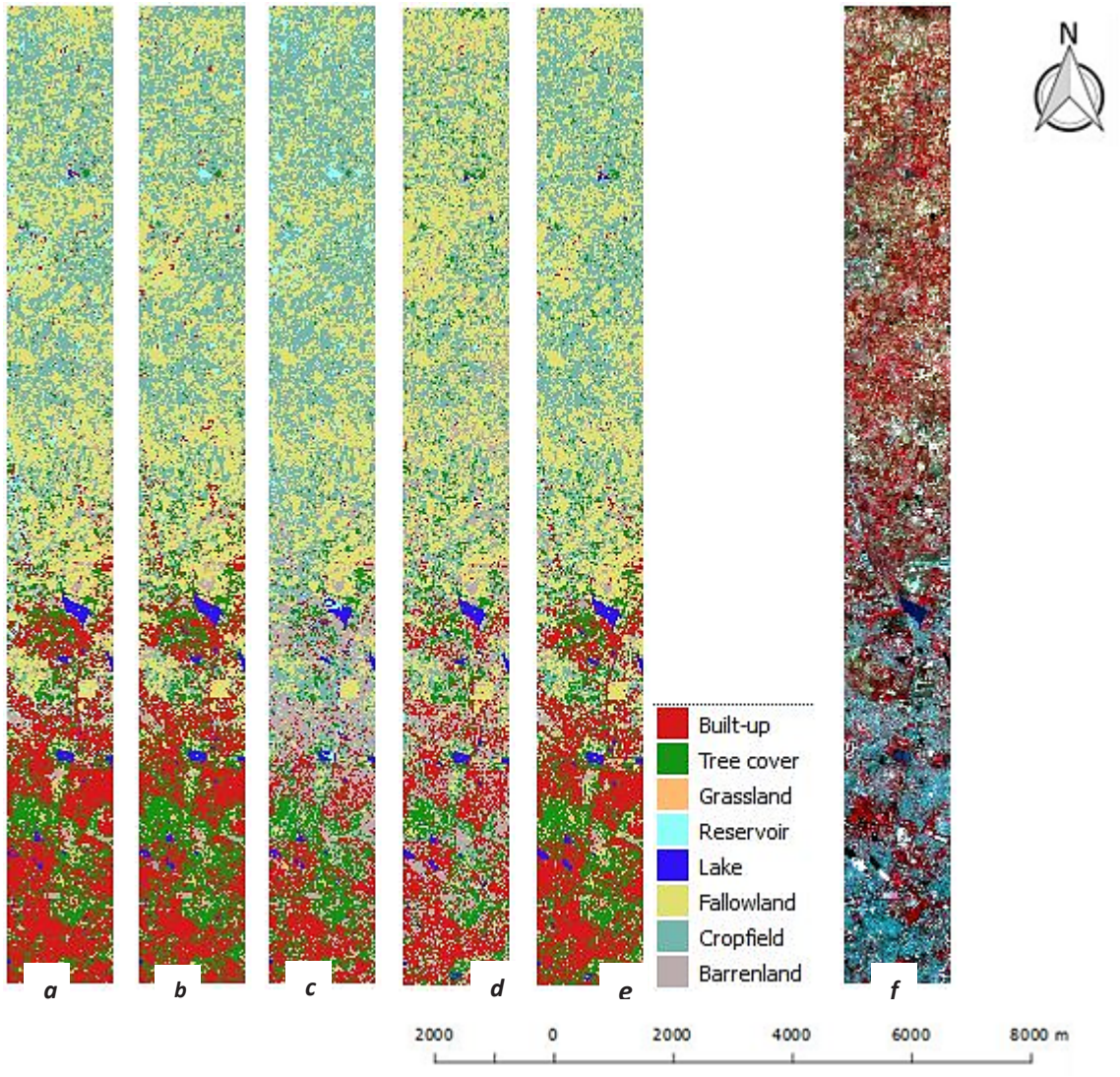

Figure 3. 3 Landsat 8 thematic maps from different classification methods (a = Unmixing #1, b = Unmixing #2, c = NAPCA, d = PCA, e = Orignal, f = Landsat 8 image)

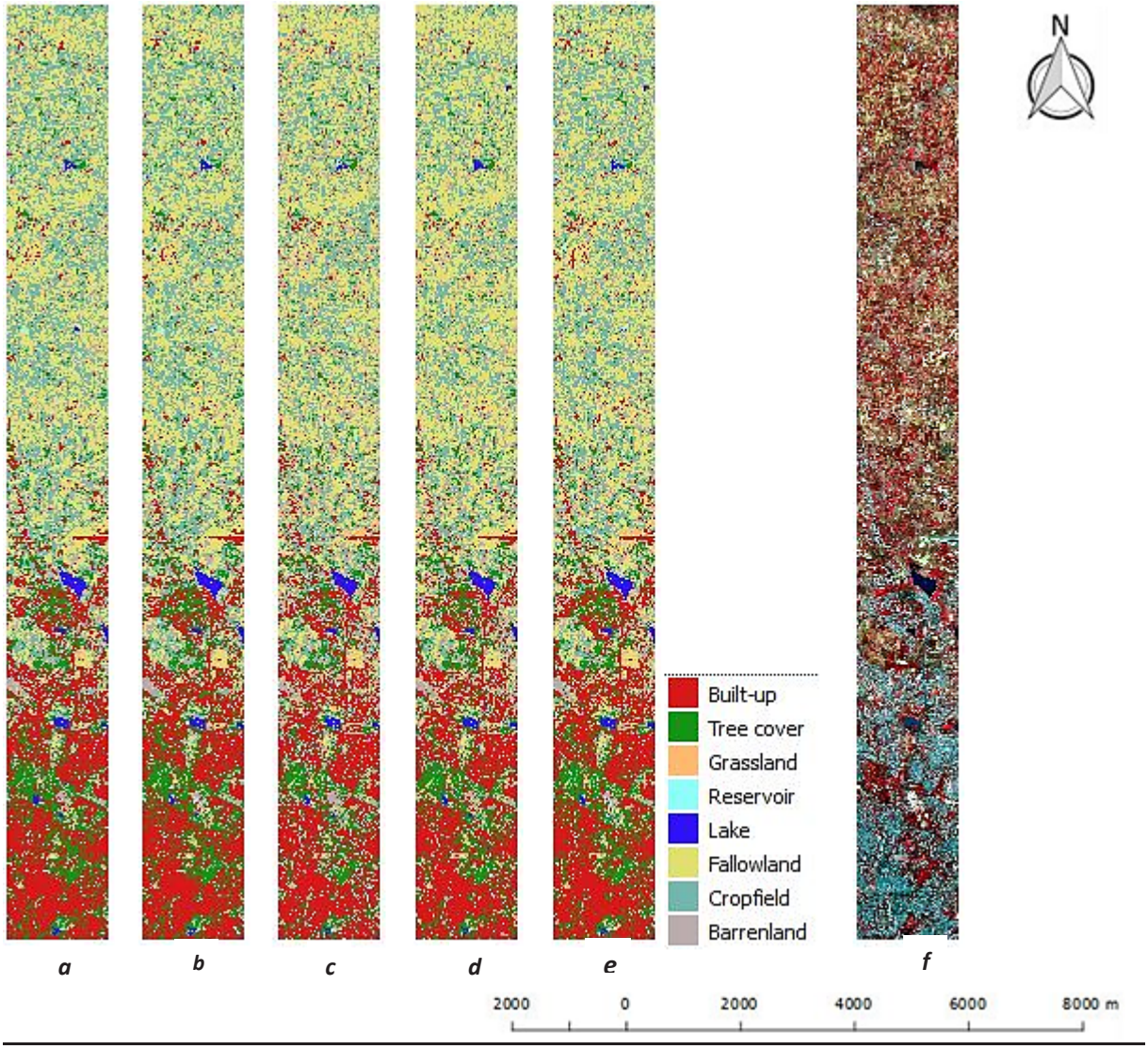

Figure 3. 4 Sentinel 2A thematic maps from different classification methods (a = Unmixing #1, b = Unmixing #2, c = NAPCA, d = PCA, e = Orignal, f = Sentinel 2A image)

A visual appraisal of the accuracy of land-cover maps in figure 3.3 (*a* to *e*) relative to the to the satellite scene (figure 3.3 *f*) clearly shows the dominance of unmixing-based feature extraction methods for land-cover classification. Conversely, the results from standard feature extraction methods (i.e. NAPCA and PCA) looks very noisy with obvious misclassification, especially within the suburban zone of the transect. This is also in resonance with the results of quantitative accuracy assessment (figure 3.8) and accuracy changes (figure 3.9) along the rural-urban transect. On the other hand, the differences in classified finer resolution Sentinel 2A image in figure 3.4 are rather subtle among the

different classification strategies. Thus emphasizing the relevance of spectral unmixing of coarser spatial resolution images.

3.2.1 Influence of Spatial Resolution on Classification Accuracy at the Rural-Urban Interface

Spatial resolution is a key consideration for minimizing spectral confusion among different land cover types and poses great consequences for image classification accuracy at the rural-urban interface. In this study, the influence of spatial resolution on classification accuracy was assessed using 30 m and 10 m Landsat 8 and Sentinel 2A satellite images respectively. Figure 3.5 shows the results of spatial resolution effects on land cover mapping at the rural-urban interface. In figure 3.5, the user's accuracy represents the proportion of all land surface features classified into a specific class, and which corresponds to the same class in the independent reference sample. Further, the producer's accuracy shows the proportion of reference areas of a particular land cover class that was correctly classified.

For most of the classes, accuracy of classification was higher at the finer spatial resolution (10 m). This trend was observed for all land cover classes in terms of producer's accuracy. A similar tendency was true for user's accuracy of all land cover classes except Grassland. In essence, the coarser resolution (30 m) proved slightly superior (i.e. averagely 4.5 %) with regards to areas correctly classified as Grassland from map user's perspective (figure 3.5). The user's accuracy for the Built-up and Fallow-land classes were high at both spatial resolutions (i.e. on average 81 % and 87 % respectively across all resolutions), with averagely 3 % and 5 % dominance of 10 m resolution over 30 m resolution respectively. The producer's accuracy for the Built-up and Fallow-land classes on the other hand shows a remarkable reduction in accuracy (i.e. on average 12 % and 28 % reduction respectively) across all spatial resolutions. For the Built-up class, producer's accuracy at 10 m resolution showed 15 % better classification accuracy than at 30 m resolution, whereas the superiority of 10 m over 30 m resolution was 6 % for the Fallow-land class. The results of user's and producer's accuracies at the different spatial resolution for the remaining classes can be inferred from figure 3.5. Overall, figure 3.5 reveals the importance of fine resolution imagery for land cover mapping at the rural-urban interface. This finding is further emphasized in figure 3.7 which shows the overall accuracy and Kappa statistics at the different spatial resolutions. For both overall accuracy and Kappa coefficients, classification accuracy reduced by approximately 10 % from 10 m to 30 m spatial resolution. Nonetheless, the results of two sample z test showed no significant differences at $p<0.05$ *(z critical = 1.96)* between the Kappa coefficients of the

different spatial resolutions (Table 3.5). Further, the result of overall disagreement between pairs of image classification outputs is shown in figure 3.6, indicates a much higher difference (i.e. 39 %) in classification results from the different resolution images.

Table 3. 5 Matrix of two sample z test showing the statistical significance between Kappa values of classification pairs

		SVM		RF	
		10 m	**30 m**	**10 m**	**30 m**
SVM	**10 m**				
	30 m	1.036			
RF	**10 m**	0.564	0.473		
	30 m	1.692	0.648	1.125	

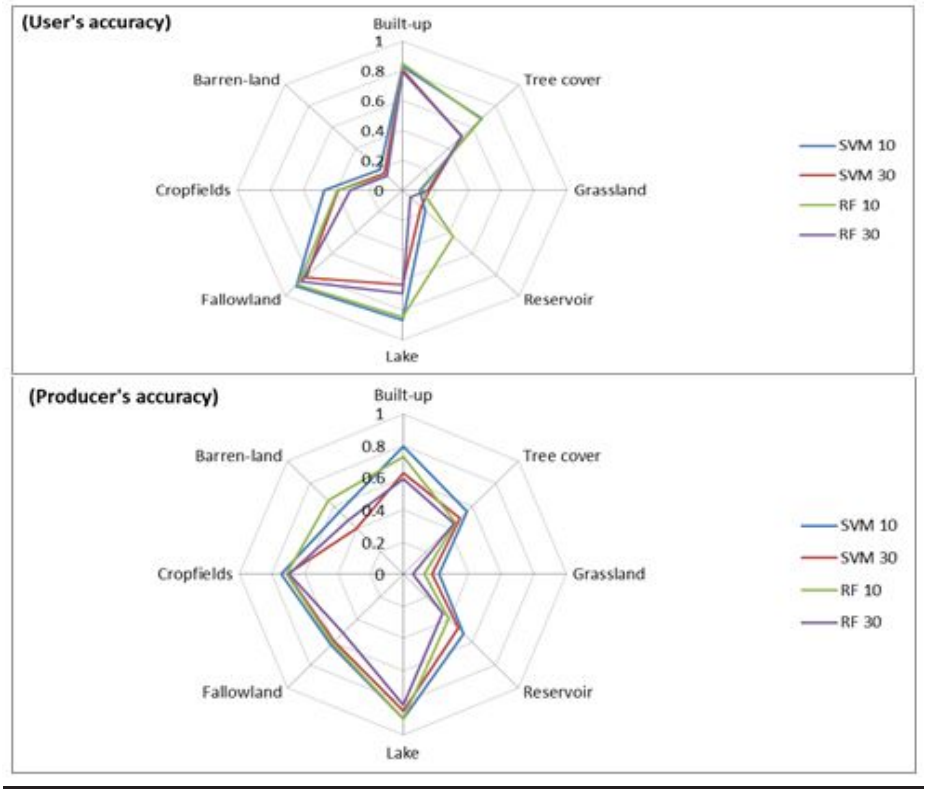

Figure 3. 5 user's and producer's accuracies of Support Vector Machines and Random Forest classifications at 10 m and 30 m resolution

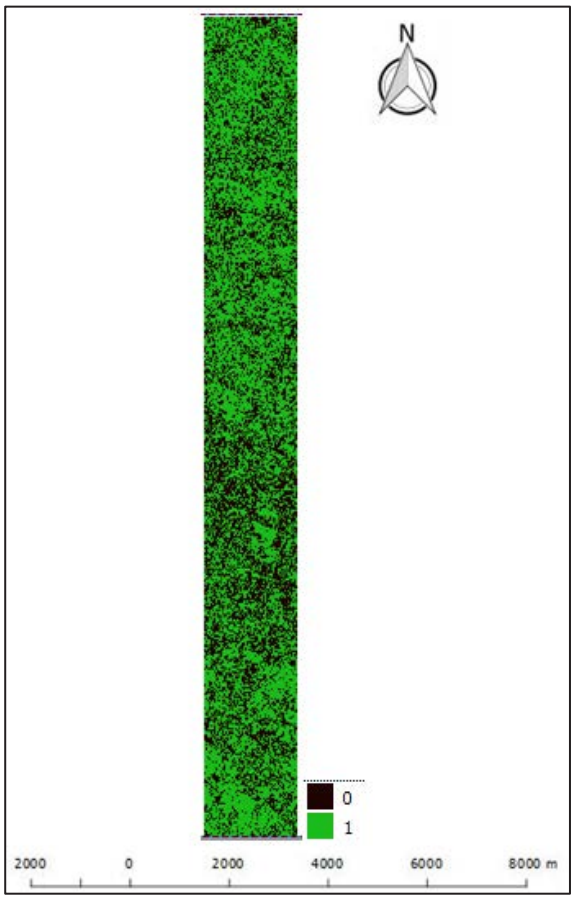

Figure 3. 6 Binary map showing the agreement between classification results at different spatial resolutions (i.e. 10 m and 30 m). The dark areas show pixels assigned to different classes (39%) while the green areas show pixels assigned to the same class (61%)

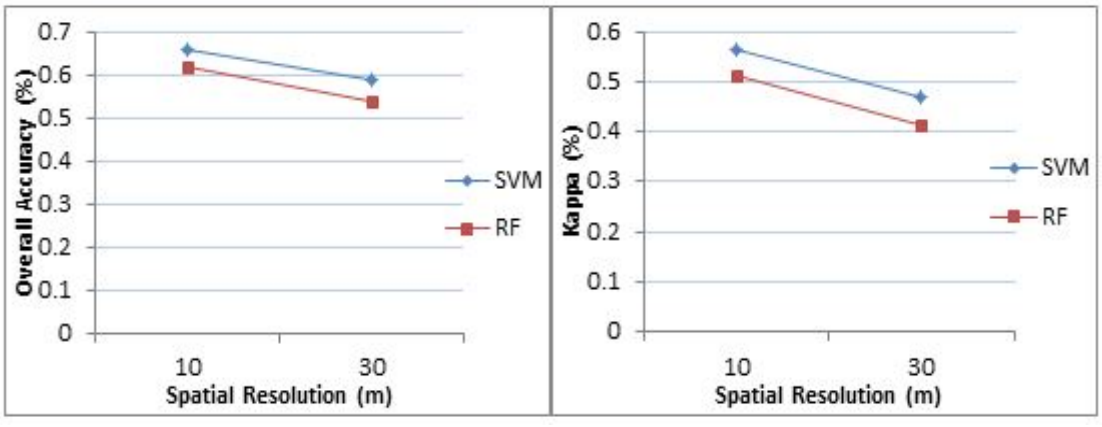

Figure 3. 7 Overall accuracy and Kappa coefficients of Support Vector Machines and Random Forest classifications at varying spatial resolutions

3.2.2 Comparison of Selected Non-Parametric Classifiers on Classification Accuracy at the Rural-Urban Interface

Non-parametric classifiers are widely recognized for their ability to handle complex classification problems (Breiman 2001; Melgani and Bruzzone 2004; Pal 2005; Rodriguez et al. 2012; Momeni et al. 2016). Evaluation of Support Vector Machine (SVM) and Random Forest (RF) classifiers was conducted to test their influence on classification accuracy at the rural-urban interface. The comparative performance of SVM and RF classifiers is presented in figure 3.7 showing a similar marginal difference in Kappa coefficients at different spatial resolutions. According to the results, SVM was 4.9 % and 5.7 % superior to RF at 10 m and 30 m spatial resolutions respectively. Even so, the z test showed no significant differences between the two classifiers both within and between the different spatial resolutions (Table 3.5). Additionally, the performance of SVM and RF classifiers was evaluated using the user's and producer's accuracies (Figure 3.5). In terms of user's accuracy, RF classifier proved only slightly better for the classification of areas identified as Built-up, Grassland and Reservoir at 10 m spatial resolution, with 2 %, 1 % and 2.3 % improvement in classification accuracy respectively. Similarly, only marginal differences in user's accuracy was observed for areas identified as Tree cover, Lake, Fallow-land, Cropfields and Barren-land (i.e. 0.7 %, 2 %, 1.5 %, 8 % and 6 % respectively) in favor of SVM classifier at 10 m spatial resolution. Reminiscent of user's accuracy at 10 m spatial resolution, user's accuracy at 30 m spatial resolution exhibited comparable differences between the two classifiers (Figure 3.5). With regards to producer's accuracy, the SVM classifier was superior at both spatial resolutions, for all thematic classes, except areas identified as Barren-land. In essence, the RF classifier improved the producer's accuracy of areas identified as Barren-land by 9.7 % and 7.2 % respectively for 10 m and 30 m spatial resolutions.

3.2.3 Performance of Unmixing-Based Feature Extraction at the Rural-Urban Interface

The feasibility of spectral unmixing for feature extraction was evaluated by comparison of a sum-to-unity constrained spectral unmixing (Figure 2.4) and partial unmixing (Figure 2.5) strategies with standard feature extraction transformations (4 components PCA and NAPCA). Hence three groups of input features (unmixing-based, original and reduced) were considered and built from the Landsat 8 and Sentinel 2A images prior to classification with Support Vector Machine (SVM). Figure 3.8 shows the results of overall accuracy and Kappa of the different feature extraction methods for Landsat 8 and Sentinel 2A images. It can be noticed that the unmixing sequences outperforms PCA and NAPCA transformations for both 30 m and 10 m resolution images (i.e. Landsat 8 and Sentinel 2A data respectively). Overall, the partial unmixing sequence (Unmixing #2) using Mixture-Tuned Match Filtering (MTMF) resulted in

the best classification accuracy results for both images (Figure 3.8), but was only marginally superior to the standard spectral unmixing sequence (Unmixing #1). Nevertheless, no statistically significant differences were observed between results of the different feature extraction methods at 95 % confidence level (*z critical = 1.96*) using two sample z test (Table 3.8).

At the level of map user's and map producer's accuracies the unmixing-based feature extraction strategies gave considerable accuracies in mapping areas identified as Built-up, Tree cover, Lakes, Fallow-lands and Cropfield, relative to original and reduced input features, particularly at finer spatial resolution (see Tables 3.6 and 3.7). Generally, areas identified as Grassland, Reservoir and Barrenland were poorly classified.

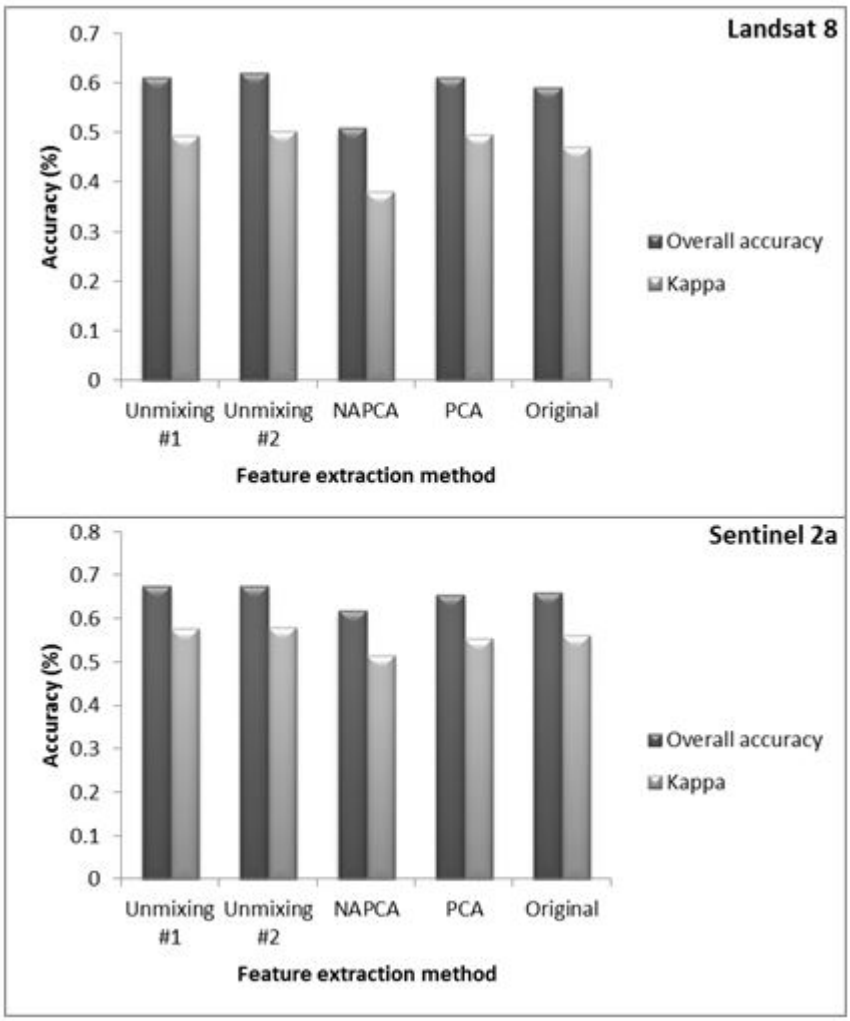

Figure 3. 8 Overall accuracy and Kappa of different feature extraction methods on Landsat 8 and Sentinel 2A images

Table 3. 6 User's and producer's accuracies for the different feature extraction methods (Unmixing-based, NAPCA, PCA and original) applied to Landsat 8 image

Class	Unmixing #1		Unmixing #2		NAPCA		PCA		Original	
	PA (%)	UA (%)	PA (%)	UA (%)	PA (%)	UA (%)	PA (%)	UA (%)	PA (%)	UA (%)
Built-up	0.68	0.77	0.63	0.78	0.35	0.80	0.72	0.77	0.63	0.80
Tree-cover	0.49	0.56	0.54	0.50	0.41	0.55	0.53	0.49	0.49	0.51
Grassland	0.19	0.18	0.12	0.20	0.08	0.15	0.06	0.09	0.17	0.16
Reservoir	0.50	0.06	0.68	0.24	0.65	0.09	0.34	0.12	0.47	0.16
Lake	0.88	0.67	0.87	0.70	0.74	0.57	0.82	0.59	0.85	0.63
Fallow-land	0.61	0.83	0.63	0.82	0.55	0.82	0.61	0.85	0.59	0.82
Cropfield	0.69	0.42	0.74	0.43	0.77	0.35	0.65	0.40	0.70	0.38
Barrenland	0.34	0.16	0.36	0.21	0.55	0.08	0.35	0.14	0.40	0.15

Table 3. 7 User's and producer's accuracies for the different feature extraction methods (Unmixing-based, NAPCA, PCA and original) applied to Sentinel 2A image

Class	Unmixing #1		Unmixing #2		NAPCA		PCA		Original	
	PA (%)	UA (%)	PA (%)	UA (%)	PA (%)	UA (%)	PA (%)	UA (%)	PA (%)	UA (%)
Built-up	0.80	0.84	0.79	0.85	0.73	0.81	0.73	0.85	0.79	0.83
Tree-cover	0.56	0.68	0.58	0.65	0.48	0.65	0.55	0.64	0.55	0.68
Grassland	0.16	0.12	0.16	0.12	0.20	0.08	0.23	0.11	0.22	0.11
Reservoir	0.48	0.16	0.53	0.16	0.39	0.09	0.41	0.16	0.53	0.20
Lake	0.93	0.85	0.89	0.83	0.88	0.92	0.88	0.83	0.90	0.87
Fallow-land	0.65	0.90	0.65	0.90	0.61	0.91	0.67	0.90	0.62	0.91
Cropfield	0.77	0.46	0.76	0.47	0.66	0.45	0.69	0.49	0.74	0.47
Barrenland	0.53	0.22	0.54	0.22	0.60	0.15	0.61	0.16	0.55	0.19

Table 3. 8 Matrix of two sample z test showing statistical differences between accuracies of different feature extraction methods for Landsat 8 and Sentinel 2A images

LANDSAT 8				
	Unmixing #1	**Unmixing #2**	**NAPCA**	**PCA**
Unmixing #2	0.09			
NAPCA	1.27	1.36		
PCA	0.01	0.07	1.29	
Original	0.26	0.36	1.00	0.28
SENTINEL 2A				
	Unmixing #1	**Unmixing #2**	**NAPCA**	**PCA**
Unmixing #2	0.015			
NAPCA	0.73	0.74		
PCA	0.28	0.29	0.44	
Original	0.19	0.20	0.54	0.09

3.2.4 Classification Accuracy Changes along the Rural-Urban Gradient

Given the apparent heterogeneity in land surface features from rural to urban areas, an assessment of the distance dependence of land cover classification accuracy was carried out to exhibit how accuracy changes along the rural-urban gradient. This was based on an equidistant (five kilometers) vertical divisions of the rural-urban transect in terms of output thematic maps and accompanying validation data. Figure 3.9 shows the trend in land cover classification accuracy (Overall accuracy and Kappa) at five-kilometer intervals from the very rural to the very urban area along the transect for Landsat 8 and Sentinel 2A images and different classification approaches. The overall classification accuracy increased marginally for the first 10 kilometers from the very rural area and thereafter decreased steadily through the remaining parts of the rural area and suburban area, reaching a lowest threshold at

approximately 11 kilometers away from the very urban area (figure 3.9). The remaining stretch of the urban area showed a sharp increase in classification accuracy and the maximum along the gradient. A similar tendency was observed for all classification approaches. As indicated in figure 3.8, the dominance of unmixing-based feature extraction strategies along the rural-urban gradient is also shown in figure 3.9. Interestingly however, the reduced input features (i.e. the PCA and NAPCA transformations) proved inferior to the original whole dimension image datasets at the finer spatial resolution (i.e. 10 m resolution Sentinel 2A image). At the coarser spatial resolution (i.e. 30 m resolution Landsat 8 image) however, the performance of PCA was comparable to the unmixing-based strategies particularly in the urban area (Figure 3.9). Yet NAPCA transformation remained the least favorable in terms of classification accuracy enhancement along the rural-urban gradient.

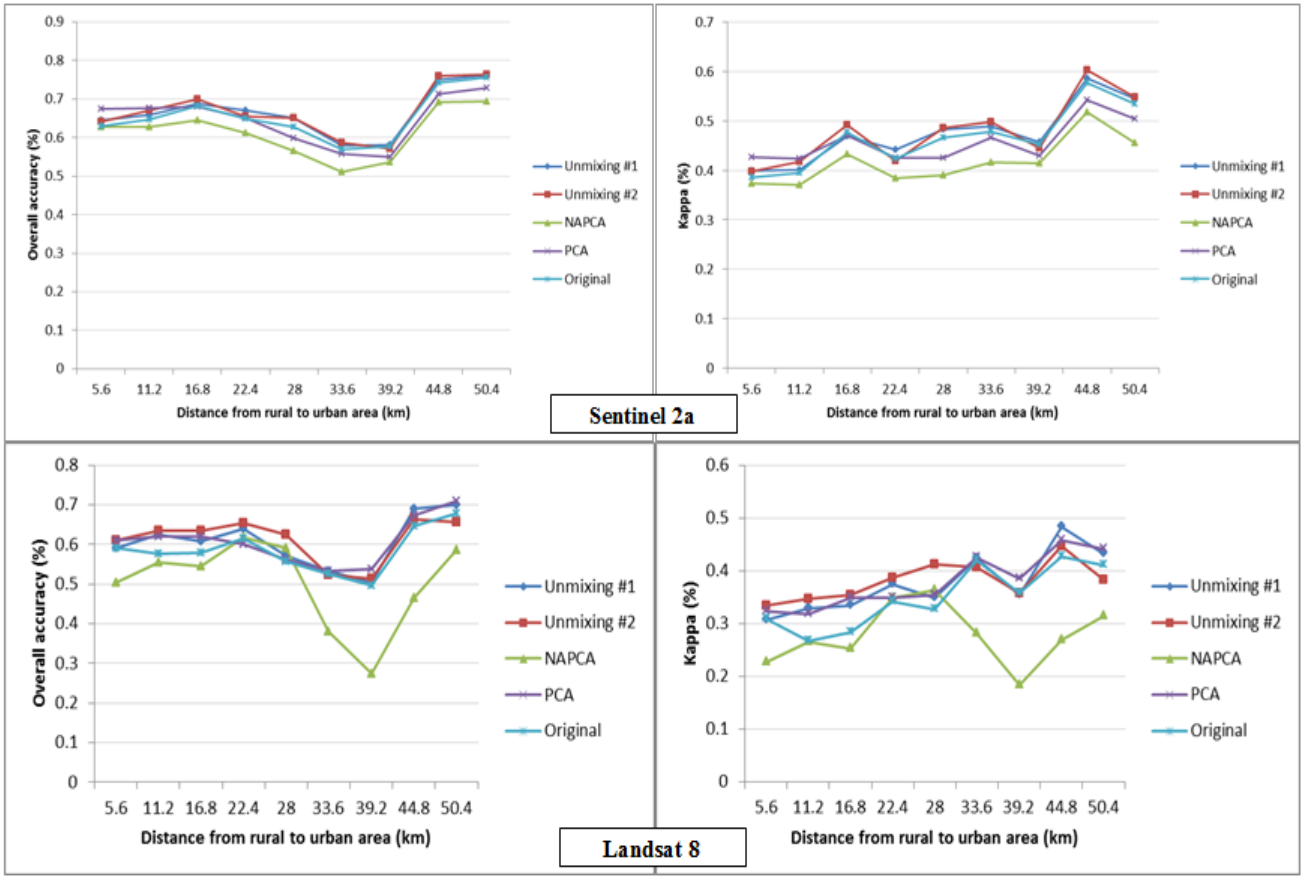

Figure 3. 9 Trend in classification accuracy changes along the rural-urban gradient for different classification approaches and spatial resolution

3.3 Land-cover Heterogeneity

3.3.1 Spectral Heterogeneity along the Rural-Urban Gradient

Assessment of spectral heterogeneity in land surface features was executed within each five-kilometer block along the rural-urban gradient using the Sequential Maximum Angle Convex Cone (SMACC) algorithm for endmember collection (see figure 2.6). Thus the degree of heterogeneity was measured as the number of endmembers returned by the SMACC algorithm.

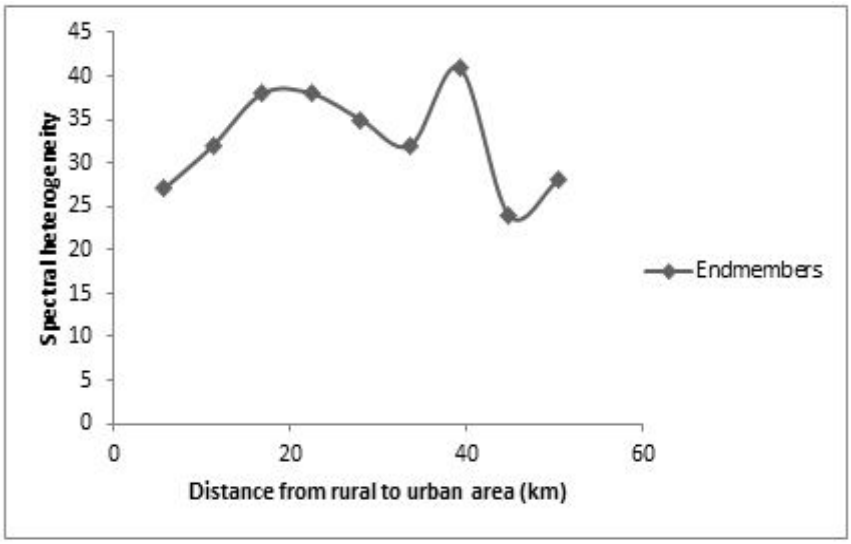

Figure 3. 10 Spectral heterogeneity along the rural-urban gradient

Figure 3.10 shows the pattern of change in degree of spectral heterogeneity in land surface features for every five kilometers along the rural-urban gradient. The number of endmembers varied considerably within each five-kilometer block from rural to urban region. Essentially, heterogeneity in land-cover increased steadily from 27 to 38 endmembers for the first 25 kilometers and reduced to 32 endmembers within the following 11 kilometers. Nonetheless block seven (11 kilometers from the very urban area) exhibited the highest degree of spectral heterogeneity (41 endmembers) while block eight (five kilometers from the very urban area) was the least heterogeneous (24 endmembers).

Among the eight identified land-cover types, the built-up class was the most spectrally heterogeneous (42 % of endmembers) along the gradient.

3.3.2 Spectral Variation within Land-cover Classes

Spectral separability analysis based on Jeffries-Matusita distance was used in the assessment of spectral variation in the same land-cover class along the rural-urban gradient. The results of per-class spectral differences between the different five-kilometer blocks along the rural-urban gradient are presented in figure 3.11. The different five-kilometer bocks are labeled from reg 1 to reg 9 (i.e. region 1 to region 9) indicating the distance differentiation from rural to urban region. Thus reg 1 and reg 9 represents the first and last five-kilometer blocks in the very rural and very urban regions respectively. The computation of spectral separability was based on the mean spectra of endmembers within each five-kilometer block that were visually identified and categorized under the same land-cover class. In essence, spectral separability of land surface features belonging to the same land-cover class was compared along the rural-urban gradient.

Overall, endmember spectra for land-cover classes namely; Built-up, Tree cover, Reservoir and Barren land were encountered in all nine five-kilometer blocks while spectra for Cropfield class were encountered in only two blocks mainly in the rural landscape (within 22 km from rural to urban area). Further, spectra for Grassland and Fallow land were recorded in seven five-kilometer blocks, with Grassland spectra mainly within urban and sub-urban landscapes whereas Fallow lands stretched from rural to sub-urban landscapes. Additionally, six blocks had endmember spectra from the Lake category.

The highest spectral distances were recorded within the Built-up and Barren-land classes with Jeffries-Matusita distances of 1.2 (between block 1 and 8) and 1.4 (between block 8 and 9) respectively while Cropfields showed no spectral differences along the gradient. Although the results of Jeffries-Matusita distance generally shows low separability thresholds, it is instructive to note that the Built-up but also the Barren land spectra in the very rural areas differed most from those in the very urban areas.

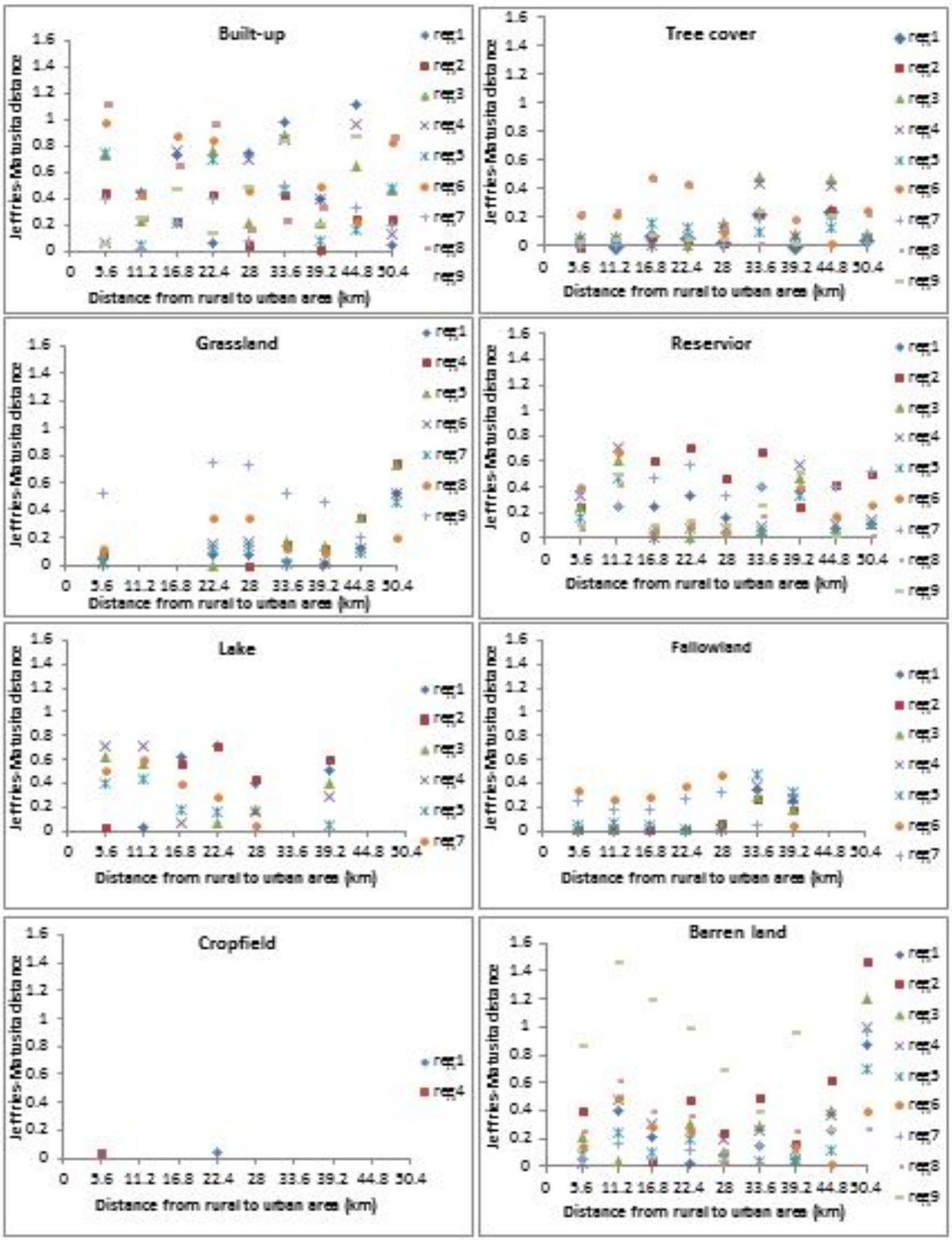

Figure 3. 11 Per-class spectral differences between the different 5 km blocks along the rural-urban gradient

3.3.3 Spatial Heterogeneity along the Rural-Urban Gradient

Figure 3.12 shows the results of spatial composition and configuration of land-cover types along the rural-urban gradient. The computed landscape metrics indicates varying spatial heterogeneity with distance from rural to urban areas at different spatial resolutions. Reminiscent of the results of spectral heterogeneity along the gradient, maximum spatial heterogeneity was observed at approximately 11 kilometers from the very urban area for all spatial metrics. Further, the results indicate a high sensitivity of PD and LSI to spatial resolution.

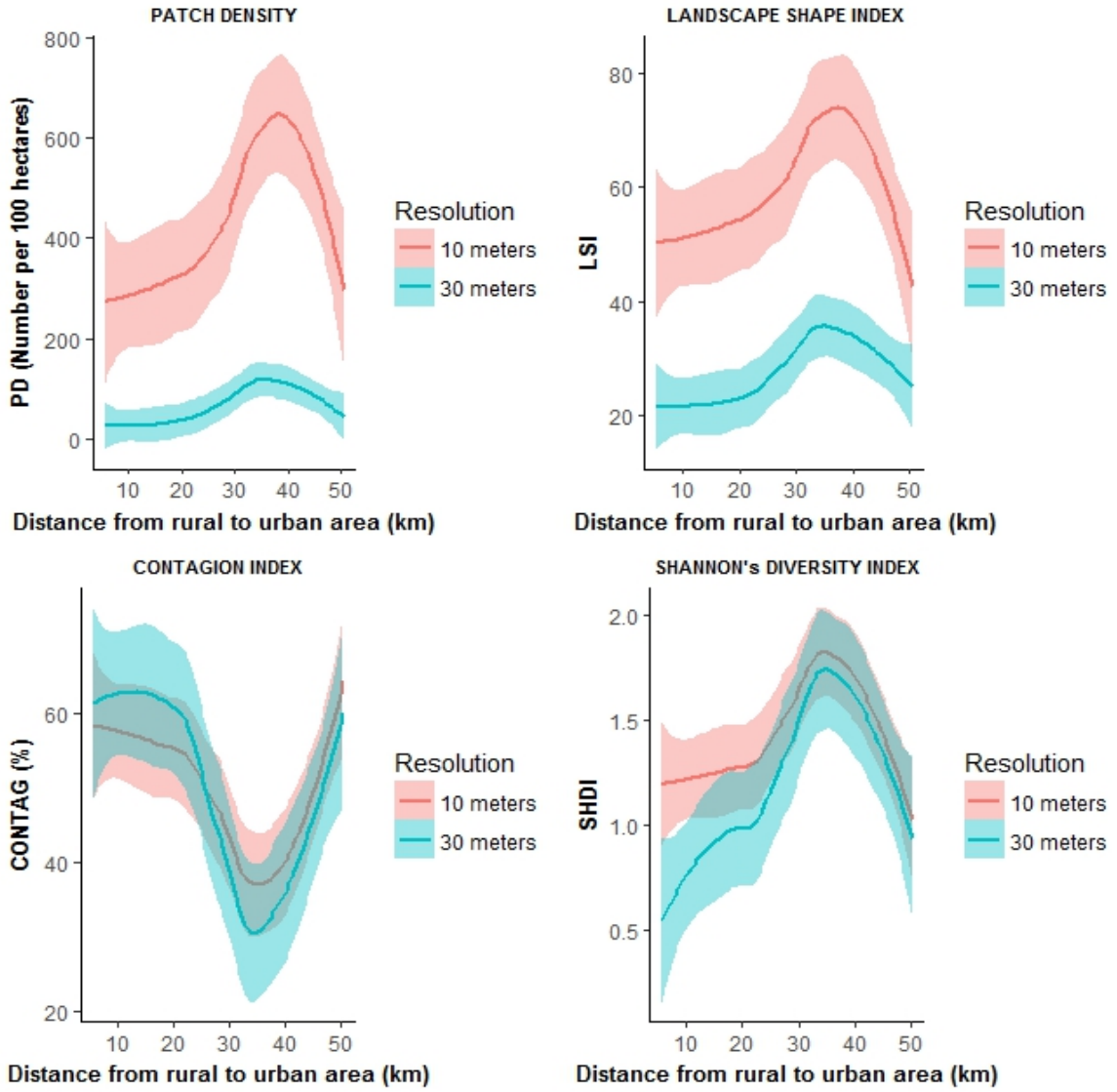

Figure 3. 12 Spatial composition and configuration from selected landscape metrics along the rural-urban gradient at different spatial resolutions

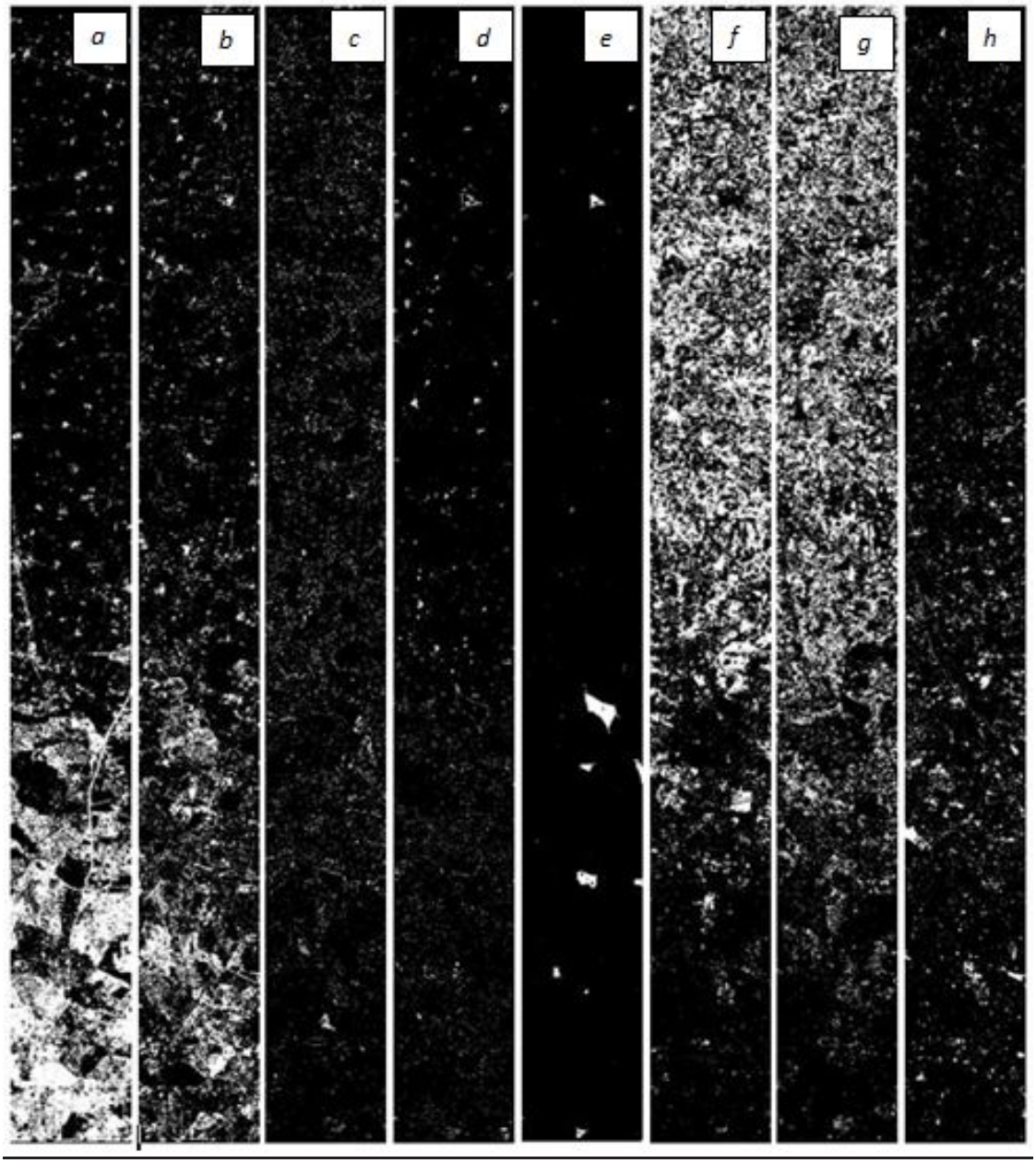

Figure 3. 13 Spatial distribution of land-cover classes classified Sentinel 2A image, (a = Built-up, b = Tree cover, c = Grassland, d = Reservoir, e = Lake, f = Fallowland, g = Cropfield, h = Barrenland)

4. Discussion

4.1 Effects of Spatial Resolution on Classification Accuracy at the Rural-Urban Interface

The results indicate that classification accuracy is influenced by image spatial resolution independent of the type of classification rule employed (figure 3.7). This general phenomenon was also observed by Huiping et al. (2003) when using pixel-based and object oriented classification approaches in their analysis of the relationship between classification accuracy, segmentation scale and image resolution. Similar findings have been reported in Ponzoni (2002), Ming et al. (2011), Suwanprasit and Srichai (2012). Generally, classification accuracy was approximately 10 % higher at the finer spatial resolution (i.e. 10 m). This result is consistent with Suwanprasit and Srichai (2012), who recorded a slight superiority in overall classification accuracy of THEOS with 15 m resolution over Landsat-5TM with 30 m resolution (i.e. 90.65 % and 89.00 % respectively). It could be inferred that the proportion of mixed pixels in the 10m Sentinel 2A image was sufficiently less than that of the 30m Landsat 8 image, and resulted in similarly less misclassified pixels. Irons et al. (1985) investigated the difficulty in classifying mixed pixels and demonstrated that percentage accuracy decreases by an average of 21 % from pure pixels. Further, this is in resonance to Rashed and Jürgens (2010)'s theory that, unique spectral signals can only be detected when spatial resolution is sufficiently fine enough to denote land surface features as pure pixels. However, contrary to the expected degree of superiority, the difference was rather insignificant at $p<0.05$ (table 4.5). To further analyze the spatial resolution effect on classification accuracy, the classified maps for the different resolution images were compared by generating a categorical binary image difference map (figure 3.5). Pixels assigned to different thematic classes in both images were reclassified as '0's while matching pixels in both maps were reclassified as '1's. From figure 3.5, the magnitude of overall disagreement between thematic maps at different spatial resolutions was found to be higher than when restricting the comparison to just overall accuracies or Kappa coefficients. For instance only ~10 % difference between overall accuracies and Kappa coefficients was observed for the classified maps of different spatial resolutions, yet, as much as 39 % same-class pixels were in disagreement when comparing the two thematic maps. The relatively high per-pixel disagreement points to the fact that overall accuracy or Kappa coefficients may not capture the spatial resolution effects on classification accuracy results in its entirety. According to Chen et al. (2004), a greater proportion of error in classification results at different spatial resolutions is concealed by the overall accuracy.

Individual class user's accuracies was highest for Built-up and Fallowland categories. Nonetheless, the producer's accuracies showed that Built-up and Fallowland categories were on average 12 % and 28 % over classified respectively. Further, the results showed only 3 % and 5% better results for the 10 m Sentinel 2A image over the 30 m Landsat 8 image respectively for these categories in terms of user's accuracy. The unique spectral features of the Built-up and Fallow-land classes was well represented in both satellite images, and in terms of user's accuracy, allowed for a more accurate classification results. Even so, the producer's accuracies revealed more dominance when using 10 m resolution image for the classification of areas identified as Built-up and Fallowlands. For areas identified as grassland, user's accuracy was higher in the 30 m resolution Landsat 8 image than the 10 m Sentinel 2A image. Similarly, Huiping et al. (2003) found that unlike small area classes like arbor which had a high accuracy when mapped from fine resolution image, large area classes like grassland had high accuracy when extracted from coarser resolution images. Generally, Hsieh and Lee (2000), Huiping et al. (2003), Chen et al. (2004) and Alshehri (2010), cautions that finer resolution images may not necessarily result in higher classification accuracy and that land cover classes exhibit different classification accuracies from different image resolutions even within the same landscape. Chen et al. (2004) recommends finer resolution images for more fragmented landscapes, while Huiping et al. (2003) iterates that different classes require different image resolutions for mapping. Ultimately, the results of this study show the suitable spatial resolution for land cover mapping at the rural-urban interface.

4.2 Comparison of Selected Non-Parametric Classifiers on Classification Accuracy at the Rural-Urban Interface

The outcome of two-sample z test (Table 3.5) showed no significant differences between classification accuracy results of SVM and RF classifiers at both spatial scales. Nonetheless the SVM classifier proved superior to the RF classifier with even a relatively bigger margin at the coarser spatial resolution. The overall dominance of SVM over RF classifier under the study conditions is in agreement with claims that SVM classifier is best at handling complex classification problems (Burai et al. 2015; Momeni et al. 2016). Moreover the result is consistent with previous studies. For example Raczko and Zagajewski (2017) recorded a similar magnitude of dominance of SVM over RF for tree species classification. Even so, some studies (e.g. Ghosh et al. 2014) report similar performance for SVM and RF classifiers or even better results for RF classifier (Li et al. 2016) in different contexts. On the level of individual class mapping, RF classifier slightly (margin of 1 % to 2.3 %) improved user's accuracies of areas identified as Built-up, Grassland and Reservoirs while SVM was better for classifying Tree cover, Lakes, Fallowlands, Cropfields. The RF classifier seems to have a good capability

of delineating land-cover classes with high inherent spectral heterogeneity (Figure 3.11) thus resulting in slightly better results in terms of user's accuracy. This could possibly be attributed to the collection of multiple tree classifiers functioning on random subsets of training samples (Breiman 2001; Li et al. 2016). However the SVM classifier leveraged improved user's accuracy results for Tree cover, Lakes, Fallowlands and Cropfields with total dominance in terms of class producer's accuracies and translated into better overall accuracy and kappa coefficient.

4.3 Performance of Unmixing-Based Feature Extraction at the Rural-Urban Interface

Mixed pixels pose a great challenge to image classification (Li et al. 2010). This is particularly true at the rural-urban interface where the landscape is characterized by a mosaic of different land cover types emanating from diverse land use scenarios (Stokman et al. 2008). Thus the potential of spectral mixture analysis for feature extraction prior to classification of Landsat 8 (30 m) and Sentinel 2A (10 m) images was evaluated by comparison with results from the original image data and standard dimensionality reduction methods (i.e. PCA and NAPCA transformations). The partial unmixing sequence using Mixture-Tuned Match Filtering was implemented due to the computational complexity and the difficulty of estimating endmembers using the standard sum-to-unity constrained linear unmixuing approach (Plaza et al. 2009). Moreover, the partial unmixing sequence offered the guarantee that highly representative endmembers were used since it incorporates information from the already defined classes. The spectral unmixing strategies improved classification accuracy at both spatial resolutions relative to the results from PCA, NAPCA and original image data, even though the differences were not significant at $p<0.05$. More specifically, the partial unmixing sequence (Unmixing #2) outperformed all tested approaches indicating that in a supervised endmember collection, focusing on spectrally pure signals may not be as important as collecting representative signatures for the predefined land cover classes (Dópido et al. 2011). For the 30 m resolution Landsat 8 image, PCA prior to classification gave the next best accuracy results after both unmixing sequences, followed by results from the full dimension image data and then NAPCA. However at 10 m spatial resolution, the standard dimensionality reduction approaches made a zero contribution to improving classification accuracy contrary to reported accuracy enhancing feature of PCA and NAPCA transformations (Howley et al. 2006; Underhill et al. 2007; Dópido et al. 2011; Dang et al. 2016). Further, the dominance of unmixing-based feature extraction methods reduced at 10 m resolution. Even so, a further study is required to ascertain the performance of image dimensionality reduction approaches at varying spatial resolutions. The accuracy enhancing feature of the unimixing-based strategies could be a function of the Minimum Noise Fraction (MNF) transformation within the processing chains (Green et al. 1988). Moreover incorporating information on the mixed

nature of pixels by means of abundance images improved the interpretability during class training leading to more accurate results (Dópido et al. 2011). Essentially, the tested unmixing sequences could provide alternatives for PCA and NAPCA transformations. Overall, areas identified s Grassland, Reservoir and Barrenland were the most poorly classified. This is explainable by the spectral confusion evident from the spectral separability assessment (table 3.4). Grasslands were largely misclassified as Cropfields while Barrenland was confused for Fallowland. This misclassification could also be a function of the size of class training samples or in combination with spectral similarity. The case of Resevoir could likely be attributed to its relatively scanty training sample size.

4.4 Effects of Land Cover Heterogeneity on Classification Accuracy along the Rural-Urban Gradient

General characteristics of landscapes such as varying spectral properties and land-cover heterogeneity have been hypothesized to hasten misclassification of pixels during image classification (Congalton 1991; Smith et al. 2002; Smith et al. 2003; Congalton and Green 2008). Thus a key part of this study was to evaluate image classification accuracy beyond the error matrix by examining pixels in the context of landscape characteristics. Landscape heterogeneity was assessed along the rural-urban gradient, spectrally using the SMACC endmember collection algorithm and spatially by quantifying landscape composition and configuration based on selected landscape metrics (i.e. PD, LSI, CONTAG and SHDI). Interestingly, there seem to be a considerable correlation between the results of spectral heterogeneity and spatial heterogeneity. As such more fragmented and spatially diverse landscapes were comparably more spectrally diverse along the rural-urban gradient. It can be inferred from the results that land-cover heterogeneity has a remarkable influence on classification accuracy. The rural and urban ends of the transect are primarily composed of agricultural lands (i.e. Fallowlands and Cropfields) and built-up surfaces respectively and were relatively more homogeneous in terms of the spectral and spatial metrics. The PD, LSI and CONTAG metrics showed the very rural and urban landscapes as having more contiguous and less fragmented patches with many liked cell adjacencies (McGarigal et al. 2002; Lechner et al. 2009) and relatively lower diversity based on SHDI. Similarly the SMACC algorithm returned relatively fewer endmembers for these areas which indicated less spectral heterogeneity. A high degree of landscape heterogeneity was observed in the peri-urban region at approximately 11 kilometers from the very urban area. This trend is also apparent from the distribution of land-cover types along the gradient (figure 3.13) where the peri-urban region (approximately 11 kilometers from the very urban area) is composed of a mixture of all land-cover types. Generally, the tendencies in accuracy changes along the rural-urban gradient are

explainable by the results from heterogeneity assessment. For example the region 11 kilometers from the very urban area had the highest degree of heterogeneity and the lowest classification accuracy. Typically the findings indicate that landscapes with high PD, LSI, SHDI and low CONTAG have lower accuracy while homogeneous and less fragmented landscapes have higher accuracy (Smith et al. 2003; Lechner et al. 2009; Tran et al. 2014).

5. Conclusions and Recommendations

5.1 Conclusions

This study examined the influence of spatial resolution, spectral unmixing techniques and land-cover heterogeneity on accuracy of land-cover mapping at the rural-urban interface in the Indian megacity of Bangalore. Analyses were performed on Landsat 8 and Sentinel 2A satellite images centered on a 50 km (vertical) by 5 km (horizontal) northern transect extending from rural to the urban center.

The results indicate that image spatial resolution plays an important role in determining the accurate classification of pixels irrespective of classification rule employed. As spatial resolution increases, the proportion of mixed pixels decreases and overall classification accuracy is enhanced. However the level of gains in classification accuracy depends on landscape composition and the method of classification applied. For example homogenous and large area classes like grassland can be mapped with a higher accuracy even at coarser spatial resolution. Moreover, classification accuracy was enhanced when using SVM classifier in comparison with RF classifier.

Further, spectral unmixing techniques for feature extraction prior to classification with SVM considerably improved classification accuracy relative to well-known PCA and NAPCA transformations. The unmixing sequences further indicates that in supervised endmember collection for spectral unmixing, representative spectral signatures from predefined land cover classes may be more important than focusing on pure signatures. Additionally, the results show that dimensionality reduction prior to classification plays little or no role in enhancing classification accuracy at finer spatial resolution. Nonetheless, this finding is subject to further investigations.

Finally, the results indicate the importance of landscape characteristics in explaining classification accuracy changes. Classification accuracy along the rural-urban gradient is inversely related to Patch Density (PD), Landscape Shape Index (LSI) and Shannon's Diversity Index (SHDI), and, directly related to Contagion Index (CONTAG). Specifically, as the degree of fragmentation and spatial diversity within a landscape increases, classification accuracy reduces. Overall, the findings from the study suggest that spatially heterogeneous landscapes exhibit high spectral variability, signaling the need to integrate spatial landscape characteristics in accuracy assessment of land-cover maps.

5.2 Recommendations

1. The major bottleneck in this study was related to computer processing of satellite images which restricted the analyses to only Landsat 8 and Sentinel 2A images leaving out the very high resolution World View 3 image. Therefore we recommended a similar study that incorporates very high resolution imagery (e.g. Worldview3) to further analyze and ascertain the influence of spatial resolution on classification accuracy at the rural-urban interface, especially in the wake of conflicting reports in available literature.

2. We proffer further studies on the effect of spatial resolution on image dimensionality reduction in terms of classification accuracy. Knowledge of this may help to design or select the optimal combination of image dimensionality reduction method and spatial resolution to enhance classification accuracy.

3. Changes in thresholds of the spatial metrics along the rural-urban gradient particularly in relation to the scale at which they are derived require to be further investigated. This study derived different spatial metrics along the rural-urban gradient and found that unlike Contagion Index (CONTAG) and Shannon's Diversity Index (SHDI), Patch Density (PD) and Landscape Shape Index (LSI) are very sensitive to spatial resolution.
4. Classification within individual 5-kilometer blocks along the rural-urban gradient gave promising results than when considering the overall transect. Thus it is recommended that where possible, image classification in similarly complex landscapes be restricted to more homogeneous micro-conditions.

ACKNOWLEDGEMENTS

I want to express my heartfelt gratitude and appreciation to Prof. Christoph Kleinn for introducing me to this interesting topic. To my immediate advisor Dr. Nils Nölke, I thank you for the guidance and assistance throughout the preparation of this thesis. I am grateful to my second advisor, Prof Eric Agestam for his motivation and the smooth administrative processes of my thesis work at the Southern Swedish Forest Research Center (SLU-Alnarp).

I would like to thank Dr Hans Fuchs and Kira Urban for the fruitful discussions and ideas during the project period, Collins Kukunda for sharing his R-scripts and the entire group at the Chair of Forest Inventory and Remote Sensing for the wonderful working environment. It was a great honour to journey with such great minds and I deeply cherish the experience.

Special acknowledgement goes to the European Commission's Erasmus Mundus SUFONAMA Scholarship program for funding my studies and stay in Europe. It has been a great opportunity to enhance my skill set and further my career. I am greatly indebted.

To my wonderful family, especially my parents Mr. Anane Emmanuel and Mrs. Amankwaa Frimpong, my brothers Amankwaa Tweneboa Kwadwo, Owusu Tweneboa Kwasi and Obah Tweneboa Emmanuel, my soul mate Josephine Sintim-Poku and mum, Uncles and Cousins, I cannot thank you enough for your prayers, encouragement and being there for me anytime I called. You forever remain close to my heart.

And finally, I dedicate this thesis to God Almighty for being the stronghold of my life and the source of my academic success.

REFERENCES

Al-doski, J., Mansor, S. B., and Shafri, H. Z. M., 2013. Image Classification in Remote Sensing*. Journal of Environment and Earth Sciences*. Vol. 3, No. 10, 2013.

Alshehri, M., 2010. The Effect of Spatial Resolution on Classification Accuracy of Marine and Coastal Areas. https://www.geospatialworld.net/article. Accessed on July 6th, 2017

Angel, S., Parent, J., Civco, D.L. and Blei, A.M., 2012. *Atlas of urban expansion*. Cambridge, MA: Lincoln Institute of Land Policy.

Bai, L., Lin, H., Sun, H., Mo, D. and Yan, E., 2012. Spectral Unmixing Approach in Remotely Sensed Forest Cover Estimation: A Study of Subtropical Forest in Southeast China. *Physics Procedia*, *25*, pp.1055-1062.

BBMP. 2010. *Namma Bangalore Nisarga: An action plan for development of Bangalore's lakes*. Bangalore: Bruhat Bangalore Mahanagara Palike.

Belousov, A.I., Verzakov, S.A. and Von Frese, J., 2002. A flexible classification approach with optimal generalisation performance: support vector machines. *Chemometrics and intelligent laboratory systems*, *64*(1), pp.15-25.

Benediktsson, J.A., Chanussot, J. and Moon, W.M., 2012. Very high-resolution remote sensing: Challenges and opportunities [point of view]. *Proceedings of the IEEE*, *100*(6), pp.1907-1910.

Benítez, P.C., McCallum, I., Obersteiner, M. and Yamagata, Y., 2004. Global supply for carbon sequestration: identifying least-cost afforestation sites under country risk consideration. IIASA, IR-04-022, Laxenburg, Austria (2004)22 pp.

Borges, J.S., Marçal, A.R.S. and Costa, J.D., 2004. Comparison of three supervised classification methods for deriving land cover maps from ASTER satellite images. *Learning*, pp.1-4.

Breiman, L., 2001. Random forests. *Machine learning*, *45*(1), pp.5-32.

Burai, P., Deák, B., Valkó, O. and Tomor, T., 2015. Classification of herbaceous vegetation using airborne hyperspectral imagery. *Remote Sensing*, *7*(2), pp.2046-2066.

Census of India. 2011. *"Rural-urban distribution" in provisional population totals, paper 2* (Vol. 1, India series 1, pp. 1–19). Viewed on 21 March 2017 (http://www.censusindia.gov.in/2011-prov-results/paper2/data_files/india/paper2_1.pdf)

Chassot, E., Bonhommeau, S., Reygondeau, G., Nieto, K., Polovina, J.J., Huret, M., Dulvy, N.K. and Demarcq, H., 2011. Satellite remote sensing for an ecosystem approach to fisheries management. *ICES Journal of Marine Science*, *68*(4), pp.651-666.

Chen, D. and Stow, D., 2002. The effect of training strategies on supervised classification at different spatial resolutions. *Photogrammetric Engineering and Remote Sensing*, *68*(11), pp.1155-1162.

Chen, D., Stow, D.A. and Gong, P., 2004. Examining the effect of spatial resolution and texture window size on classification accuracy: an urban environment case. *International Journal of Remote Sensing*, *25*(11), pp.2177-2192.

Cohen, J. 1960. A Coefficient of Agreement for Nominal Scales. Educational and Psychological Measurement, 20, 37-46.

Congalton, R.G. and Green, K., 2008. Assessing the accuracy of remotely sensed data: principles and practices. *CRC press*

Congalton, R.G., 1991. A review of assessing the accuracy of classifications of remotely sensed data. *Remote sensing of environment*, *37*(1), pp.35-46.

Congalton, R.G., 2001. Accuracy assessment and validation of remotely sensed and other spatial information. *International Journal of Wildland Fire*, *10*(4), pp.321-328.

Cushnie, J.L., 1987. The interactive effect of spatial resolution and degree of internal variability within land-cover types on classification accuracies. International Journal of Remote Sensing, 8(1), pp.15-29.

Dabboor, M., Howell, S., Shokr, M. and Yackel, J., 2014. The Jeffries–Matusita distance for the case of complex Wishart distribution as a separability criterion for fully polarimetric SAR data. *International Journal of Remote Sensing*, *35*(19), pp.6859-6873.

Dang, T.H., Pham, T.D., Tran, H.L. and Le Van, Q., 2016. October. Using dimension reduction with feature selection to enhance accuracy of tumor classification. In *Biomedical Engineering (BME-HUST), International Conference on* (pp. 14-17). IEEE.

Dash, J. and Ogutu, B.O., 2016. Recent advances in space-borne optical remote sensing systems for monitoring global terrestrial ecosystems. *Progress in Physical Geography*, *40*(2), pp.322-351.

De Smith, M.J., Goodchild, M.F. and Longley, P., 2007. *Geospatial analysis: a comprehensive guide to principles, techniques and software tools*. Troubador Publishing Ltd.

Dópido, I., Zortea, M., Villa, A., Plaza, A. and Gamba, P., 2011. Unmixing prior to supervised classification of remotely sensed hyperspectral images. *IEEE Geoscience and Remote Sensing Letters*, *8*(4), pp.760-764.

Exelis Visual Information Solutions, 2014. ENVI Classic Tutorial: Using SMACC to Extract Endmembers.

Foody G. and Mathur A. 2004. Toward intelligent training of supervised image classifications: directing training data acquisition for SVM classification. Remote Sensing of Environment 93 (2004) 107–117

Foody, G.M. 2004. Thematic map comparison: evaluating the statistical significance of differences in classification accuracy *Photogrammetric Engineering and Remote Sensing*, 70, (5), pp. 627-633.

Foody, G.M., 2002. Status of land-cover classification accuracy assessment. *Remote sensing of environment*, *80*(1), pp.185-201.

Foody, G.M., Mathur, A., Sanchez-Hernandez, C. and Boyd, D.S., 2006. Training set size requirements for the classification of a specific class. *Remote Sensing of Environment*, *104*(1), pp.1-14.

Fritz, S., See, L., McCallum, I., Schill, C., Obersteiner, M., Van der Velde, M., Boettcher, H., Havlík, P. and Achard, F., 2011. Highlighting continued uncertainty in global land cover maps for the user community. *Environmental Research Letters*, *6*(4), p.044005.

Gayathri, S., Latha, N. and Mohan, M.R., 2013. Impact of Climate Change on Water Quality of Shoolkere Lake, Bangalore. *Journal of Academia and Industrial Research (JAIR)*, *2*(6), pp.362-368.

Ghosh, A., Fassnacht, F.E., Joshi, P.K. and Koch, B., 2014. A framework for mapping tree species combining hyperspectral and LiDAR data: Role of selected classifiers and sensor across three spatial scales. *International Journal of Applied Earth Observation and Geoinformation*, *26*, pp.49-63.

Goetz, S.J., Wright, R.K., Smith, A.J., Zinecker, E. and Schaub, E., 2003. IKONOS imagery for resource management: Tree cover, impervious surfaces, and riparian buffer analyses in the mid-Atlantic region. Remote sensing of environment, 88(1), pp.195-208.

Green, A.A., Berman, M., Switzer, P. and Craig, M.D., 1988. A transformation for ordering multispectral data in terms of image quality with implications for noise removal. *IEEE Transactions on geoscience and remote sensing*, *26*(1), pp.65-74.

Gruninger, J.H., Ratkowski, A.J. and Hoke, M.L., 2004. August. The sequential maximum angle convex cone (SMACC) endmember model. In *Defense and Security* (pp. 1-14). International Society for Optics and Photonics.

Hackman, K.O., Gong, P. and Wang, J., 2017. New land-cover maps of Ghana for 2015 using Landsat 8 and three popular classifiers for biodiversity assessment. *International Journal of Remote Sensing*, *38*(14), pp.4008-4021.

Hamedianfar, A., Shafri, H.Z.M., Mansor, S. and Ahmad, N., 2014. Improving detailed rule-based feature extraction of urban areas from WorldView-2 image and lidar data. *International Journal of Remote Sensing*, *35*(5), pp.1876-1899.

Hiremath, S., Prabhuraj, D. K., Lakshmikantha, B. P. and Chakraborty, S. D., 2013. Land Use/Land Cover Change Analysis of Bangalore Urban District and Its Impact on Land Surface Temperature. *ISRS Conference paper*. December 4-6, 2013.

Howley, T., Madden, M.G., O'Connell, M.L. and Ryder, A.G., 2006. The effect of principal component analysis on machine learning accuracy with high-dimensional spectral data. *Knowledge-Based Systems*, *19*(5), pp.363-370.

Hsieh, P.F. and Lee, L.C., 2000. Effect of spatial resolution on classification error in remote sensing. In *Geoscience and Remote Sensing Symposium, 2000. Proceedings. IGARSS 2000. IEEE 2000 International* (Vol. 1, pp. 171-173). IEEE.

Huiping, H., Bingfang, W. and Jinlong, F., 2003, July. Analysis to the relationship of classification accuracy, segmentation scale, image resolution. In *Geoscience and Remote Sensing Symposium, 2003. IGARSS'03. Proceedings. 2003 IEEE International* (Vol. 6, pp. 3671-3673). Ieee.

Hussin, Y.A. and Atmopawiro, V.P., 2004. Sub-pixel and maximum likelihood classification of landsat ETM+ images for detecting illegal logging and mapping tropical rain forest cover types in berau, east Kalimantan, Indonesia. In *Unknown*.

Indian Meteorological Department 2013. Rainfall statistics of India. HYDROMET DIVISION. Available at http://hydro.imd.gov.in/hydrometweb/(S(c1illuqiw2h03kyy4arlfju0))/PRODUCTS/Publications/Rainfall%20Statistics%20of%20India%20-%202013/Rainfall%20Statistics%20of%20India%20-%202013.pdf Accessed on 15th June 2017

Irons, J.R., Markham, B.L., Nelson, R.F., Toll, D.L., Williams, D.L., Latty, R.S. and Stauffer, M.L., 1985. The effects of spatial resolution on the classification of Thematic Mapper data. *International Journal of Remote Sensing*, *6*(8), pp.1385-1403.

Jensen, J.R., 2015. Introductory Digital Image Processing: A Remote Sensing Perspective. Prentice Hall Press Upper Saddle River, NJ, USA ©2015, pp 110-205

Kamphaus, B.D., 2014. *Automated mapping of sub-pixel impervious surface area from landsat imagery*. State University of New York at Buffalo.

Keerthi, S.S. and Lin, C.J., 2003. Asymptotic behaviors of support vector machines with Gaussian kernel. *Neural computation*, *15*(7), pp.1667-1689.

Keshava, N. and Mustard, J.F., 2002. Spectral unmixing. *IEEE signal processing magazine*, *19*(1), pp.44-57.

Khorram, S., van der Wiele, C.F., Koch, F.H., Nelson, S.A. and Potts, M.D., 2016. Future Trends in Remote Sensing. In *Principles of Applied Remote Sensing* (pp. 277-285). Springer International Publishing.

Lechner, A.M., Stein, A., Jones, S.D. and Ferwerda, J.G., 2009. Remote sensing of small and linear features: quantifying the effects of patch size and length, grid position and detectability on land cover mapping. *Remote Sensing of Environment*, *113*(10), pp.2194-2204.

Li, X., Chen, W., Cheng, X. and Wang, L., 2016. A comparison of machine learning algorithms for mapping of complex surface-mined and agricultural landscapes using ZiYuan-3 stereo satellite imagery. *Remote Sensing*, *8*(6), p.514.

Li, X., Ling, F. and Du, Y., 2010. June. Characterizing sub-pixel landscape patterns from remotely sensed imagery with sub-pixel mapping methods. In *Geoinformatics, 2010 18th International Conference on* (pp. 1-5). IEEE.

Liming Bai , Hui Lin, Hua Sun, Dengkui Mo, Enping Yan, 2012. Spectral Unmixing Approach in Remotely Sensed Forest Cover Estimation: A Study of Subtropical Forest in Southeast China. Physics Procedia 25 (2012) 1055 – 1062

Lu, D. and Weng, Q., 2005. Urban classification using full spectral information of Landsat ETM+ imagery in Marion County, Indiana. *Photogrammetric Engineering & Remote Sensing*, *71*(11), pp.1275-1284.

Lu, D. and Weng, Q., 2007. A survey of image classification methods and techniques for improving classification performance. *International journal of Remote sensing*, *28*(5), pp.823-870.

Lu, D. and Weng, Q., 2009. Extraction of urban impervious surfaces from an IKONOS image. *International Journal of Remote Sensing*, *30*(5), pp.1297-1311.

Lu, D., Hetrick, S. and Moran, E., 2010. Land cover classification in a complex urban-rural landscape with QuickBird imagery. *Photogrammetric Engineering & Remote Sensing*, *76*(10), pp.1159-1168.

MacLean, M.G. and Congalton, R.G., 2012. March. Map accuracy assessment issues when using an object-oriented approach. In *Proceedings of the American Society for Photogrammetry and Remote Sensing 2012 Annual Conference* (pp. 1-5).

Mallinis, G., Koutsias, N., Tsakiri-Strati, M. and Karteris, M., 2008. Object-based classification using Quickbird imagery for delineating forest vegetation polygons in a

Mediterranean test site. *ISPRS Journal of Photogrammetry and Remote Sensing*, *63*(2), pp.237-250.

Marjanović, M., Kovačević, M., Bajat, B. and Voženílek, V., 2011. Landslide susceptibility assessment using SVM machine learning algorithm. *Engineering Geology*, *123*(3), pp.225-234.

Mather, P.M. 1999. Computer Processing of Remotely Sensed Images: An Introduction, 2nd ed.; Wiley: Chichester, UK.

Mathieu, R. and Aryal, J., 2007. Object-based classification of Ikonos imagery for mapping large-scale vegetation communities in urban areas. *Sensors*, *7*(11), pp.2860-2880.

McCoy, R.M. 2005. Field Methods in Remote Sensing; Guilford Press: New York, NY, USA.

McGarigal, K. and Marks, B.J., 1995. Spatial pattern analysis program for quantifying landscape structure. *Gen. Tech. Rep. PNW-GTR-351. US Department of Agriculture, Forest Service, Pacific Northwest Research Station*.

McGarigal, K., Cushman, S.A., Neel, M.C. and Ene, E., 2002. FRAGSTATS: spatial pattern analysis program for categorical maps. Viewed on 21 March 2017 (http://www.umass.edu/landeco/research/fragstats/fragstats.html)

Melgani, F. and Bruzzone, L., 2004. Classification of hyperspectral remote sensing images with support vector machines. *IEEE Transactions on geoscience and remote sensing*, *42*(8), pp.1778-1790.

Ming, D., Yang, J., Li, L. and Song, Z., 2011. Modified ALV for selecting the optimal spatial resolution and its scale effect on image classification accuracy. *Mathematical and Computer Modelling*, *54*(3), pp.1061-1068.

Momeni, R., Aplin, P. and Boyd, D.S., 2016. Mapping complex urban land cover from spaceborne imagery: The influence of spatial resolution, spectral band set and classification approach. *Remote Sensing*, *8*(2), p.88.

Mora, B., Tsendbazar, N.E., Herold, M. and Arino, O., 2014. Global land cover mapping: Current status and future trends. In *Land Use and Land Cover Mapping in Europe* (pp. 11-30). Springer Netherlands.

Nagendra, H. and Gopal, D., 2011. Tree diversity, distribution, history and change in urban parks: studies in Bangalore, India. *Urban Ecosystems*, *14*(2), pp.211-223.

Nesbitt, L. and Meitner, M.J., 2016. Exploring Relationships between Socioeconomic Background and Urban Greenery in Portland, OR. *Forests*, *7*(8), p.162.

Nong, D.H., Fox, J., Miura, T. and Saksena, S., 2015. Built-up Area Change Analysis in Hanoi Using Support Vector Machine Classification of Landsat Multi-Temporal Image Stacks and Population Data. *Land*, *4*(4), pp.1213-1231.

Pacifici, F., Chini, M. and Emery, W.J., 2009. A neural network approach using multi-scale textural metrics from very high-resolution panchromatic imagery for urban land-use classification. *Remote Sensing of Environment*, *113*(6), pp.1276-1292.

Pal, M., 2005. Random forest classifier for remote sensing classification. *International Journal of Remote Sensing*, *26*(1), pp.217-222.

Plaza, A., Benediktsson, J.A., Boardman, J.W., Brazile, J., Bruzzone, L., Camps-Valls, G., Chanussot, J., Fauvel, M., Gamba, P., Gualtieri, A. and Marconcini, M., 2009. Recent advances in techniques for hyperspectral image processing. *Remote sensing of environment*, *113*, pp.S110-S122.

Ponzoni, F.J., Galvão, L.S. and Epiphanio, J.C., 2002. Spatial resolution influence on the identification of land cover classes in the Amazon environment. *Anais da Academia Brasileira de Ciências*, *74*(4), pp.717-725.

Puissant, A., Hirsch, J. and Weber, C., 2005. The utility of texture analysis to improve per-pixel classification for high to very high spatial resolution imagery. *International Journal of Remote Sensing*, *26*(4), pp.733-745.

QGIS Development Team, 2017. QGIS Geographic Information System. *Open Source Geospatial Foundation Project*. http://www.qgis.org/

Quintano, C., Fernández-Manso, A. and Roberts, D.A., 2013. Multiple Endmember Spectral Mixture Analysis (MESMA) to map burn severity levels from Landsat images in Mediterranean countries. *Remote Sensing of Environment*, *136*, pp.76-88.

R Core Team, 2016. R: A language and environment for statistical computing. R Foundation for Statistical Computing, Vienna, Austria. URL https://www.R-project.org/.

Raczko, E. and Zagajewski, B., 2017. Comparison of support vector machine, random forest and neural network classifiers for tree species classification on airborne hyperspectral APEX images. *European Journal of Remote Sensing*, *50*(1), pp.144-154.

Rashed, T. and Jürgens, C. eds., 2010. *Remote sensing of urban and suburban areas* (Vol. 10). Springer Science & Business Media.

Richards, J. A. and Jia, X., 2006. Remote Sensing Digital Image Analysis: An Introduction. Berlin, Germany: Springer

Rodriguez-Galiano, V.F., Ghimire, B., Rogan, J., Chica-Olmo, M. and Rigol-Sanchez, J.P., 2012. An assessment of the effectiveness of a random forest classifier for land-cover classification. *ISPRS Journal of Photogrammetry and Remote Sensing*, *67*, pp.93-104.

Schüle, S.A., Gabriel, K.M. and Bolte, G., 2017. Relationship between neighbourhood socioeconomic position and neighbourhood public green space availability: An environmental inequality analysis in a large German city applying generalized linear models. *International Journal of Hygiene and Environmental Health*.

Sertel, E., Robock, A. and Ormeci, C., 2010. Impacts of land cover data quality on regional climate simulations. *International Journal of Climatology*, *30*(13), pp.1942-1953.

Shaban, M.A. and Dikshit, O., 2001. Improvement of classification in urban areas by the use of textural features: the case study of Lucknow city, Uttar Pradesh. *International Journal of Remote Sensing*, *22*(4), pp.565-593.

Shannon, C.E. and Weaver, W., 1949. The mathematical theory of information. University of Illinois Press, Urbana, IL

Simon, D., 2008. Urban environments: issues on the peri-urban fringe. *Annual review of environment and resources*, *33*.

Small, C., 2001. Estimation of urban vegetation abundance by spectral mixture analysis. *International journal of remote sensing*, *22*(7), pp.1305-1334.

Smith, J.H., Stehman, S.V., Wickham, J.D. and Yang, L., 2003. Effects of landscape characteristics on land-cover class accuracy. *Remote Sensing of Environment*, *84*(3), pp.342-349.

Smith, J.H., Wickham, J.D., Stehman, S.V. and Yang, L., 2002. Impacts of patch size and land-cover heterogeneity on thematic image classification accuracy. *Photogrammetric Engineering and Remote Sensing*, *68*(1), pp.65-70.

Sohn, Y. and McCoy, R.M., 1997. Mapping desert shrub rangeland using spectral unmixing and modeling spectral mixtures with TM data. *Photogrammetric Engineering and Remote Sensing*, *63*(6), pp.707-716.

Stokman, A., Rabe, S. and Ruff, S., 2008. Beijing's New Urban Countryside–Designing with Complexity and Strategic Landscape Planning. *Journal of Landscape Architecture*, *3*(2), pp.30-45.

Sudha, P. and Ravindranath, N.H., 2000. A study of Bangalore urban forest. *Landscape and Urban Planning*, *47*(1), pp.47-63.

Sudhira, H.S. and Nagendra, H., 2013. Local assessment of Bangalore: graying and greening in Bangalore–Impacts of urbanization on ecosystems, ecosystem services and biodiversity. In *Urbanization, Biodiversity and Ecosystem Services: Challenges and Opportunities* (pp. 75-91). Springer Netherlands.

Sugumaran, R., Zerr, D. and Prato, T., 2002. Improved urban land cover mapping using multi-temporal IKONOS images for local government planning. *Canadian Journal of Remote Sensing*, *28*(1), pp.90-95.

Suwanprasit, C. and Srichai, N., 2012. Impacts of spatial resolution on land cover classification. *Proceedings of the Asia-Pacific Advanced Network*, *33*, pp.39-47.

Tran, T.V., Julian, J.P. and de Beurs, K.M., 2014. Land cover heterogeneity effects on sub-pixel and per-pixel classifications. *ISPRS International Journal of Geo-Information*, *3*(2), pp.540-553.

Underhill D.G., McDowell, L.K., Marchette, D.J. and Solka, J.L., 2007, August. Enhancing text analysis via dimensionality reduction. In *Information Reuse and Integration, 2007. IRI 2007. IEEE International Conference* (pp. 348-353). IEEE.

Van der Sande, C.J., De Jong, S.M. and De Roo, A.P.J., 2003. A segmentation and classification approach of IKONOS-2 imagery for land cover mapping to assist flood risk and flood damage assessment. *International Journal of applied earth observation and geoinformation*, *4*(3), pp.217-229.

Van Niel, T.G., McVicar, T.R. and Datt, B., 2005. On the relationship between training sample size and data dimensionality: Monte Carlo analysis of broadband multi-temporal classification. *Remote Sensing of Environment*, *98*(4), pp.468-480.

Vapnik, V., 2013. *The nature of statistical learning theory*. Springer science & business media.

Woodcock, C.E. and Gopal, S., 2000. Fuzzy set theory and thematic maps: accuracy assessment and area estimation. *International Journal of Geographical Information Science*, *14*(2), pp.153-172.

Wu, W., Shibasaki, R., Yang, P., Ongaro, L., Zhou, Q. and Tang, H., 2008. Validation and comparison of 1 km global land cover products in China. *International Journal of Remote Sensing*, *29*(13), pp.3769-3785.

Yu, Q., Gong, P., Clinton, N., Biging, G., Kelly, M. and Schirokauer, D., 2006. Object-based detailed vegetation classification with airborne high spatial resolution remote sensing imagery. *Photogrammetric Engineering & Remote Sensing*, *72*(7), pp.799-811.

Zhang, J. and Foody, G.M., 2001. Fully-fuzzy supervised classification of sub-urban land cover from remotely sensed imagery: statistical and artificial neural network approaches. *International journal of remote sensing*, *22*(4), pp.615-628.

Zhou, W., Troy, A. and Grove, M., 2008. Object-based land cover classification and change analysis in the Baltimore metropolitan area using multitemporal high resolution remote sensing data. *Sensors*, *8*(3), pp.1613-1636.

APPENDICES

Appendix I Error matrices for Landsat 8 thematic maps

A. Error matrix for unmixing sequence 1

		PREDICTED LABELS									
	Class	**1**	**2**	**3**	**4**	**5**	**6**	**7**	**8**	**Totals**	**PAs**
REFERENCE LABELS	**1**	4152	714	77	486	46	131	258	215	6079	0.683007
	2	723	1782	208	42	22	334	377	100	3588	0.496656
	3	152	135	150	33	11	110	56	138	785	0.191083
	4	20	7	3	61	14	2	10	3	120	0.508333
	5	6	8	2	9	204	0	2	0	231	0.883117
	6	124	104	173	190	3	6559	3052	437	10642	0.616332
	7	40	343	153	13	2	652	2771	26	4000	0.69275
	8	136	36	26	59	0	50	33	181	521	0.347409
	Totals	5353	3129	792	893	302	7838	6559	1100	25966	
	UAs	0.77564	0.569511	0.189394	0.068309	0.675497	0.836821	0.422473	0.164545		
							OA	**0.610799**		**kappa**	**0.494822**

B. Error matrix for unmixing sequence 2

		PREDICTED LABELS									
	Class	**1**	**2**	**3**	**4**	**5**	**6**	**7**	**8**	**Totals**	**PAs**
REFERENCE LABELS	**1**	3847	1130	40	116	36	439	265	206	6079	0.632834
	2	594	1961	119	4	30	255	541	84	3588	0.546544
	3	134	221	100	3	11	156	65	95	785	0.127389
	4	8	6	3	82	4	0	15	2	120	0.683333
	5	13	8	0	7	201	0	2	0	231	0.87013
	6	149	137	129	104	1	6748	3053	321	10642	0.634091
	7	32	334	80	11	0	535	2995	13	4000	0.74875
	8	123	52	21	14	1	89	29	192	521	0.368522
	Totals	4900	3849	492	341	284	8222	6965	913	25966	
	UAs	0.785102	0.509483	0.203252	0.240469	0.707746	0.820725	0.430007	0.210296		
							OA	**0.621043**		**kappa**	**0.503206**

C. Error matrix for NAPCA transformation

		PREDICTED LABELS									
	Class	**1**	**2**	**3**	**4**	**5**	**6**	**7**	**8**	**Totals**	**PAs**
REFERENCE LABELS	**1**	2151	717	55	314	77	320	472	1973	6079	0.353841
	2	363	1475	52	54	31	244	1049	320	3588	0.411093
	3	55	127	64	15	4	145	154	221	785	0.081529
	4	11	6	1	78	1	2	16	5	120	0.65
	5	6	6	1	36	172	0	7	3	231	0.744589
	6	22	48	126	292	5	5884	3902	363	10642	0.552904
	7	3	236	98	41	1	473	3110	38	4000	0.7775
	8	47	36	5	22	6	57	59	289	521	0.554702
	Totals	2658	2651	402	852	297	7125	8769	3212	25966	
	UAs	0.809255	0.556394	0.159204	0.091549	0.579125	0.825825	0.354658	0.089975		
							OA	**0.509243**		**kappa**	**0.382105**

D. Error matrix for PCA transformation

		PREDICTED LABELS									
	Class	**1**	**2**	**3**	**4**	**5**	**6**	**7**	**8**	**Totals**	**PAs**
REFERENCE LABELS	**1**	4386	788	12	134	63	252	246	198	6079	0.7215
	2	667	1907	26	54	37	196	639	62	3588	0.531494
	3	181	167	54	23	8	110	141	101	785	0.06879
	4	14	31	1	41	12	6	8	7	120	0.341667
	5	12	17	0	8	191	0	2	1	231	0.82684
	6	189	190	304	39	4	6512	2728	676	10642	0.611915
	7	21	661	189	3	2	456	2630	38	4000	0.6575
	8	163	54	3	29	2	48	36	186	521	0.357006
	Totals	5633	3815	589	331	319	7580	6430	1269	25966	
	UAs	0.778626	0.499869	0.091681	0.123867	0.598746	0.859103	0.40902	0.146572		
							OA	**0.612609**		**kappa**	**0.496428**

E. Error matrix for full dimension image

		PREDICTED LABELS									
	Class	**1**	**2**	**3**	**4**	**5**	**6**	**7**	**8**	**Totals**	**PAs**
REFERENCE LABELS	**1**	3840	887	111	159	49	308	289	436	6079	0.631683
	2	586	1770	225	35	35	299	522	116	3588	0.493311
	3	108	144	138	19	6	142	84	144	785	0.175796
	4	16	7	5	57	15	2	17	1	120	0.475
	5	13	6	4	8	197	0	2	1	231	0.852814
	6	61	95	189	60	4	6308	3520	405	10642	0.592746
	7	23	505	127	7	3	481	2832	22	4000	0.708
	8	102	56	25	10	2	79	38	209	521	0.401152
	Totals	4749	3470	824	355	311	7619	7304	1334	25966	
	UAs	0.808591	0.510086	0.167476	0.160563	0.633441	0.82793	0.387733	0.156672		
							OA	**0.591196**		**kappa**	**0.471146**

F. Error matrix for RF classification

		PREDICTED LABELS									
	Class	**1**	**2**	**3**	**4**	**5**	**6**	**7**	**8**	**Totals**	**PAs**
REFERENCE LABELS	**1**	3598	478	12	310	40	340	612	689	6079	0.591874
	2	566	1590	35	92	26	99	1055	125	3588	0.443144
	3	129	92	48	40	3	73	243	157	785	0.061146
	4	9	27	1	41	10	5	23	4	120	0.341667
	5	6	19	0	10	188	0	6	2	231	0.813853
	6	105	123	113	83	2	5477	4123	616	10642	0.514659
	7	27	747	96	11	3	301	2789	26	4000	0.69725
	8	109	23	4	20	1	57	60	247	521	0.474088
	Totals	4549	3099	309	607	273	6352	8911	1866	25966	
	UAs	0.790943	0.513069	0.15534	0.067545	0.688645	0.862248	0.312984	0.132369		
							OA	**0.538319**		**kappa**	**0.413639**

Appendix II Error matrices for Sentinel 2A thematic maps

A. Error matrix for unmixing sequence 1

		PREDICTED LABELS									
	Class	**1**	**2**	**3**	**4**	**5**	**6**	**7**	**8**	**Totals**	**PAs**
REFERENCE LABELS	**1**	4848	416	64	183	2	170	215	191	6089	0.8
	2	495	2023	124	54	1	107	760	29	3593	0.56
	3	127	69	122	16	2	146	226	78	786	0.16
	4	11	8	1	58	33	1	2	6	120	0.48
	5	0	3	0	12	217	0	1	0	233	0.93
	6	105	61	458	31	1	6954	2394	667	10671	0.65
	7	14	395	226	8	0	261	3095	9	4008	0.77
	8	138	8	11	2	0	55	30	277	521	0.53
	Totals	5738	2983	1006	364	256	7694	6723	1257	26021	
	UAs	0.844894	0.678176	0.121272	0.159341	0.847656	0.903821	0.46036	0.220366		
							OA	**0.676146**		**kappa**	**0.578989**

B. Error matrix for unmixing sequence 2

		PREDICTED LABELS									
	Class	**1**	**2**	**3**	**4**	**5**	**6**	**7**	**8**	**Totals**	**PAs**
REFERENCE LABELS	**1**	4827	493	109	186	3	155	129	187	6089	0.79
	2	463	2101	146	47	1	114	691	30	3593	0.58
	3	126	80	128	20	2	147	210	73	786	0.16
	4	5	8	0	64	33	5	2	3	120	0.53
	5	2	1	0	21	208	0	1	0	233	0.89
	6	121	79	440	36	4	6949	2373	669	10671	0.65
	7	11	429	212	9	0	267	3056	24	4008	0.76
	8	127	23	16	7	0	53	15	280	521	0.54
	Totals	5682	3214	1051	390	251	7690	6477	1266	26021	
	UAs	0.849525	0.653703	0.121789	0.164103	0.828685	0.903641	0.471823	0.221169		
							OA	**0.676876**		**kappa**	**0.580339**

C. Error matrix for NAPCA transformation

		PREDICTED LABELS									
	Class	**1**	**2**	**3**	**4**	**5**	**6**	**7**	**8**	**Totals**	**PAs**
REFERENCE LABELS	**1**	4455	215	136	337	1	131	171	643	6089	0.73
	2	564	1742	212	97	1	121	786	70	3593	0.48
	3	122	59	157	10	1	104	178	155	786	0.2
	4	24	6	1	47	16	2	2	22	120	0.39
	5	3	8	0	17	205	0	0	0	233	0.88
	6	180	51	863	14	0	6554	2129	880	10671	0.61
	7	34	597	486	1	0	210	2652	28	4008	0.66
	8	100	5	21	8	0	47	27	313	521	0.6
	Totals	5482	2683	1876	531	224	7169	5945	2111	26021	
	UAs	0.81266	0.649273	0.083689	0.088512	0.915179	0.914214	0.446089	0.148271		
							OA	**0.619692**		**kappa**	**0.515108**

D. Error matrix for PCA transformation

		PREDICTED LABELS									
	Class	**1**	**2**	**3**	**4**	**5**	**6**	**7**	**8**	**Totals**	**PAs**
REFERENCE LABELS	**1**	4422	350	180	186	3	167	107	674	6089	0.73
	2	459	1971	185	30	1	161	732	54	3593	0.55
	3	102	65	177	5	1	127	159	150	786	0.23
	4	17	8	1	49	35	3	1	6	120	0.41
	5	3	4	0	21	205	0	0	0	233	0.88
	6	90	51	742	11	1	7132	1865	779	10671	0.67
	7	14	604	359	0	0	255	2756	20	4008	0.69
	8	108	9	19	5	0	43	21	316	521	0.61
	Totals	5215	3062	1663	307	246	7888	5641	1999	26021	
	UAs	0.847939	0.643697	0.106434	0.159609	0.833333	0.904158	0.488566	0.158079		
							OA	**0.654395**		**kappa**	**0.554368**

E. Error matrix for full dimension image

		PREDICTED LABELS									
	Class	**1**	**2**	**3**	**4**	**5**	**6**	**7**	**8**	**Totals**	**PAs**
REFERENCE LABELS	**1**	4837	460	144	146	3	135	110	254	6089	0.79
	2	520	1987	219	30	2	96	699	40	3593	0.55
	3	145	61	171	15	2	122	170	100	786	0.22
	4	8	13	0	63	25	6	1	4	120	0.53
	5	1	3	0	18	210	0	1	0	233	0.9
	6	169	34	698	34	0	6651	2317	768	10671	0.62
	7	32	355	357	1	0	267	2975	21	4008	0.74
	8	133	9	21	11	0	46	15	286	521	0.55
	Totals	5845	2922	1610	318	242	7323	6288	1473	26021	
	UAs	0.82754491	0.680014	0.106211	0.198113	0.867769	0.908234	0.473123	0.194162		
							OA	**0.660236**		**kappa**	**0.562248**

F. Error matrix for RF classification

		PREDICTED LABELS									
	Class	**1**	**2**	**3**	**4**	**5**	**6**	**7**	**8**	**Totals**	**PAs**
REFERENCE LABELS	**1**	4450	134	20	26	4	203	558	694	6089	0.730826
	2	382	1644	46	8	1	124	1366	22	3593	0.457556
	3	133	45	103	4	2	122	247	130	786	0.131043
	4	19	6	1	47	31	1	9	6	120	0.391667
	5	5	4	0	13	210	0	1	0	233	0.901288
	6	153	31	433	8	0	6512	2218	1316	10671	0.610252
	7	17	577	271	0	0	275	2848	20	4008	0.710579
	8	87	3	7	2	0	56	29	337	521	0.646833
	Totals	5246	2444	881	108	248	7293	7276	2525	26021	
	UAs	0.848265	0.672668	0.116913	0.435185	0.846774	0.892911	0.391424	0.133465		
							OA	**0.620691**		**kappa**	**0.512942**

Appendix III Initial land-cover map for determining degree of urbanness based on Landsat 8 image.